Available online at www.sciencedirect.com
SCIENCE DIRECT®
Geochimica et Cosmochimica Acta 70 (2006) 1231–1260
Geochimica
www.elsevier.com/locate/gca

Trace element distribution in peridotite xenoliths from Tok, SE Siberian craton: A record of pervasive, multi-stage metasomatism in shallow refractory mantle

Dmitri A. Ionov [a,b,c,d,*], Gilles Chazot [c], Catherine Chauvel [d], Claude Merlet [b], Jean-Louis Bodinier [b]

[a] *Max-Planck-Institut für Chemie, Postfach 3060, D-55020 Mainz, Germany*
[b] *Laboratoire de Tectonophysique (UMR 5568 CNRS), Université Montpellier 2, 34095 Montpellier, France*
[c] *Université Blaise Pascal, 63038 Clermont-Ferrand, France*
[d] *LGCA, Maison des Géosciences, Université de Grenoble, 38041 Grenoble, France*

Received 6 June 2005; accepted in revised form 7 November 2005

Abstract

Spinel peridotite xenoliths in alkali basalts at Tok, SE Siberian craton range from fertile lherzolites to harzburgites and wehrlites; olivine-rich (70–84%) rocks are dominant. REE patterns in the lherzolites range from nearly flat for fertile rocks (14–17% cpx) to LREE-enriched; the enrichments are positively correlated with modal olivine, consistent with high-permeability of olivine-rich rocks during melt percolation. Clinopyroxene in olivine-rich Tok peridotites typically has convex-upward trace element patterns ($La/Nd_{PM} < 1$ and $Nd/Yb_{PM} \gg 1$), which we consider as evidence for equilibration with evolved silicate liquids (with higher REE and lower Ti contents than in host basalts). Whole-rock patterns of the olivine-rich xenoliths range from convex-upward to LREE-enriched ($La/Nd_{PM} > 1$); the LREE-enrichments are positively correlated with phosphorus abundances and are mainly hosted by accessory phosphates and P-rich cryptocrystalline materials. In addition to apatite, some Tok xenoliths contain whitlockite (an anhydrous, halogen-poor and Na–Mg-rich phosphate), which is common in meteorites and lunar rocks, but has not been reported from any terrestrial mantle samples. Some olivine-rich peridotites have generations of clinopyroxene with distinct abundances of Na, LREE, Sr and Zr. The mineralogical and trace element data indicate that the lithospheric mantle section represented by the xenoliths experienced a large-scale metasomatic event produced by upward migration of mafic silicate melts followed by percolation of low-*T*, alkali-rich melts and fluids. Chromatographic fractionation and fractional crystallisation of the melts close to the percolation front produced strong LREE-enrichments, which are most common in the uppermost mantle and are related to carbonate- and P_2O_5-rich derivatives of the initial melt. Reversal and gradual retreat of the percolation front during thermal relaxation to ambient geotherm (''retrograde'' metasomatism) caused local migration and entrapment of small-volume residual fluids and precipitation of volatile-rich accessory minerals. A distinct metasomatic episode, which mainly produced ''anhydrous'' late-stage interstitial materials was concomitant with the alkali basaltic magmatism, which brought the xenoliths to the surface.

1. Introduction

Mantle metasomatism is a complex enrichment phenomenon that may involve chemical equilibration of minerals in host peridotites with percolating fluids (cryptic metasomatism), changes in the modal composition of the host (re-fertilisation) and precipitation of accessory phases rich in incompatible elements (modal metasomatism). We use a combination of high-resolution imaging, in situ and whole-rock analyses to unravel the contributions of those processes to metasomatism in mantle xenoliths from the South-Eastern (SE) Siberian craton.

Spinel peridotite xenoliths in alkali basaltic rocks in the Tokinsky Stanovik Range near the southern rim of the

* Corresponding author. Fax: +49 69 798 25183.
E-mail address: ionov@em.uni-frankfurt.de (D.A. Ionov).

0016-7037/$ - see front matter © 2005 Elsevier Inc. All rights reserved.
doi:10.1016/j.gca.2005.11.010

Aldan shield (referred to as Tok here) provide the only currently available samples of the lithospheric mantle in the SE part of the Siberian craton (Ionov et al., 2005c,e). The Tok xenoliths are fragments of the shallow mantle (likely 40–60 km) and the only known suite of mantle peridotites on the Siberian craton hosted by Cenozoic basalts. By contrast, kimberlite-borne xenoliths from the northern and central Siberian craton mainly represent deeper lithosphere and are hosted by older (Paleozoic to early Mesozoic) volcanic rocks. In the Mesozoic and Cenozoic, the Tok domain was the active SE margin of Siberia facing the NW Pacific and experienced several major tectono-magmatic events.

The Tok xenoliths are large and fresh; they yield an excellent material for whole-rock and in situ analyses, in stark contrast to the usually strongly altered xenoliths from kimberlites. We report here, trace element and mineralogical data for samples (Table 1) that were the subject of detailed petrographic and major element studies (Ionov et al., 2005c,e). Trace elements in 45 xenoliths are determined by inductively coupled plasma mass-spectrometry (ICPMS). Whole-rock samples are analysed by solution ICPMS; minerals are analysed by laser-ablation (LA) ICPMS. Clinopyroxene (cpx) in one sample is analysed by secondary ion mass-spectrometry (SIMS). We also use electron probe micro-beam analysis (EPMA) to study accessory metasomatic hosts of incompatible elements.

Petrographic and major element data (Ionov et al., 2005c,e) show ubiquitous effects of mantle metasomatism on refractory Tok peridotites, which appear to be more widespread and strong than in many other mantle xenolith suites worldwide. The goal of this study is to explore trace element and mineralogical effects of the metasomatism. Our specific objectives are to: (1) identify and characterise major and accessory hosts of trace elements; (2) constrain relative contributions of individual phases to trace element budgets of whole-rocks; (3) define trace element features of main rock types and relate them to petrographic and major element data; (4) outline the role of depletion by partial melting and later enrichments in trace element budgets; (5) identify enrichment episodes, their mechanisms and sources; (6) outline the relations of the metasomatic events to tectonic settings and lithospheric history. Collectively, these data are used to further constrain the nature of mantle metasomatism worldwide.

2. Analytical methods

Major element compositions of minerals were determined in thin sections by EPMA on a CAMECA SX-100 instrument equipped with five wavelength-dispersive X-ray spectrometers (WDS) at Service Microsonde Sud (Université Montpellier 2). The analyses were done with 20 kV accelerating voltage, a focused beam of 10 nA and counting times of 20–30 s. Concentrations are obtained from raw intensities using the "X-PHI" quantification procedure (Merlet, 1994). Natural minerals, synthetic oxides and pure metals are used as standards. Phosphates were also analysed for Sr, La, Ce and Nd using 25 kV voltage, defocused beam of 30 nA and counting times of 60–120 s. Some micro-phases were identified with Raman micro-spectroscopy at J. Gutenberg University (Mainz) on LabRAM HR800 Jobin–Yvon Horiba spectrometer using an He–Ne laser beam at $\lambda = 632.8$ nm (1.96 eV) with a diameter of 1–2 μm and 3 mW power (Tichomirowa et al., 2005).

Pyroxenes, amph and phl were analysed for trace elements by LA-ICPMS in Clermont–Ferrand in grain mounts (polished 25 mm epoxy disks) and in 200 μm thick polished rock sections. The ICPMS instrument is a VG PlasmaQuad2+ coupled with an UV (266 nm) Q-switched Nd-YAG laser source operating at 4 Hz. The pulse energy is about 2 mJ, the size of the beam is ~60 μm. Argon is used as carrier gas. The background was measured for 50 s and then the signal was acquired for 100 s. Data reduction was performed with the GLITTER software. Reference sample SRN NIST 612 was used as external standard (Pearce et al., 1997), with ^{44}Ca as internal standard for cpx and amph and ^{29}Si for phl. Detection limits are between 0.1 and 0.5 ppm for Sc, V and Pb and below 0.01–0.04 ppm for other elements. Precision and accuracy (<10% and <5%, respectively) were assessed from repeated analyses of reference sample BCR-2 G (Norman, 1998; Raczek et al., 2001; Eggins, 2003). In addition, three cpx, 18 opx and 23 ol were analysed on a Finnigan Element-2 magnetic sector ICPMS instrument coupled with an automated UP-213 Nd-YAG LA-microprobe at MPI für Chemie in Mainz. The analyses were done in low-resolution mode, with ^{43}Ca and ^{30}Si as internal standards using SRM NIST 612 for external calibration (Ionov et al., 2005a). Cpx in one sample was analysed by SIMS on an upgraded Cameca 4f ion probe in Montpellier following procedures reported by Bottazzi et al., 1994.

Whole-rock trace element compositions were determined by solution ICPMS at Grenoble University generally following the technique of Eggins et al. (1997). Finely ground rock powders (~100 mg) were dissolved in HF–$HClO_4$ mixtures. Dried samples were taken up in HNO_3 and diluted to 1:1000 (in 2% HNO_3) shortly before the analysis. Sample solutions were spiked with As, Tm and Bi. Reference sample BHVO-1 was used for calibration. Spiked solutions were analysed on a Fisons (VG-Elemental) PQ2+Turbo (PlasmaQuad II+) instrument. Chemical blanks and 2–3 reference materials (BIR-1, BEN, UB-N and JP-1) were run with each sample batch. These data agree well with a small number of duplicate analyses done earlier in other laboratories (Ionov et al., 2005c,e); they include data for more elements than earlier analyses done at Bristol (Ionov et al., 2005e).

3. Textural position and mineralogy of metasomatic products

Three rock series are identified among Tok peridotites based on petrography and Mg# [$Mg/(Mg + Fe)_{at}$]

Table 1
Sample list with a summary of modal data, Mg# in olivine, Cr# in spinel and *T* estimates

Sa. No.	Rock type	Mg# ol	Cr# spl	Calculated modal abundances, wt.%							*T* (°C) Ca-opx
				ol	opx	cpx	spl	fs	ap	other	
Lherzolite–harzburgite (LH) series peridotites											
1–2	Harzburgite	0.913	0.64	78.6	17.2	3.1	0.3	0.7	0.12		910
1–3	Harzburgite	0.912	0.64	80.1	13.4	5.0	0.3	1.1			907
1–13	Harzburgite	0.910	0.48	80.1	15.6	2.7	0.6	0.9		+	933
2–6	Low-cpx lh	0.899	0.44	67.4	25.4	5.6	0.6	0.9			980
2–9	Harzburgite	0.914	0.62	79.2	15.7	3.1	0.5	1.5			874
3–4	Harzburgite	0.910	0.38	73.7	20.9	3.3	0.7			(phl?)	910
3–19	Low-cpx lh	0.900	0.34	70.5	21.1	6.2	0.8	1.3			931
5–3	Lherzolite	0.904	0.27	73.7	15.2	9.4	0.0	1.5	0.24		907
6–0	Harzburgite	0.919	0.41	79.9	14.9	2.8	0.6	1.5	0.34		890
6–1	Lherzolite	0.895	0.08	54.6	25.8	17.0	2.5				1010
6–2	Lherzolite	0.895	0.09	53.9	26.3	17.3	2.5				1001
6–3	Lherzolite	0.909	0.20	54.6	33.2	10.2	1.0	0.8			976
7–1	Low-cpx lh	0.911	0.55	78.6	15.1	5.0	0.4	0.8			985
7–5	Lherzolite	0.901	0.12	57.2	26.5	14.2	2.1				985
8–1	Low-cpx lh	0.904	0.27	73.6	17.5	6.7	1.0	1.3		(phl?)	1005
8–2	Low-cpx lh	0.906	0.34	74.1	18.8	5.8	0.7	0.6			976
8–3	Harzburgite	0.903	0.46	73.5	20.3	4.1	0.5	1.5		(phl?)	956
8–5	Lherzolite	0.901	0.14	63.4	24.1	10.5	1.6	0.4		(phl?)	1004
8–6	Lherzolite	0.896	0.10	59.4	22.5	15.1	2.3	0.6			985
8–7	Harzburgite	0.911	0.55	76.8	16.7	4.8	0.5	1.1	0.12	(am?)	968
8–8	Harzburgite	0.911	0.47	72.0	22.7	3.7	0.6	1.0		(am?)	955
8–11	Harzburgite	0.913	0.54	77.6	17.5	4.5	0.4				957
8–31	Harzburgite	0.916	0.56	76.5	16.6	4.8	0.4	1.7	0.15	crypt.	887
8–39	Lherzolite	0.894	0.09	53.9	26.3	17.2	2.6				964
8–40	Harzburgite	0.913	0.57	71.3	24.0	3.7	0.5		0.41	(am?)	922
8–50	Harzburgite	0.912	0.40	77.1	17.6	3.6	0.7	0.9			992
10–2	Harzburgite	0.915	0.59	77.2	16.6	4.3	0.4	1.3	0.12		914
10–4	Harzburgite	0.914	0.57	79.9	16.0	2.7	0.4	1.0		crypt.	926
10–8	Harzburgite	0.908	0.54	79.2	14.9	4.9	0.4	0.6		crypt.	950
10–16	Low-cpx lh	0.899	0.51	76.2	17.4	6.0	0.4				957
10–17	Harzburgite	0.907	0.24	75.6	19.5	3.6	1.3				1011
10–19	Harzburgite	0.911	0.46	72.7	22.8	3.4	0.7		0.30		951
Lherzolite–wehrlite (LW) series peridotites											
2–1	Wehrlite	0.870	0.41	78.3	0.9	19.5	0.3	0.9			
2–2	Wehrlite	0.884	0.42	79.0	4.4	13.6	0.6	2.4			909
2–3	Low-opx lh	0.884	0.32	79.6	5.2	11.9	0.7	2.5		am	908
2–4	Wehrlite	0.880	0.31	80.3	1.0	15.4	0.6	2.6	0.13	am	
2–10	Low-opx lh	0.882	0.10	66.4	10.5	18.1	2.5	2.4		(phl?)	1024
3–2	Low-opx lh	0.890	0.40	75.9	5.9	15.2	0.8			(phl?)	949
3–22	Wehrlite	0.860	0.54	82.3	tr.	15.8	0.3	1.4	0.13	crypt.	
8–10	Wehrlite	0.877	0.26	79.1	1.1	16.6	0.9	2.3	0.13		984
10–1	Wehrlite	0.857	0.14	71.5	2.9	22.4	1.5	1.6			964
10–3	Wehrlite	0.842	0.63	84.2	tr.	15.6	0.1				982
10–11	Lherzolite	0.851	0.47	78.2	12.6	7.4	0.4	1.1	0.42		920
Olivine–cpx cumulate											
8–14	ol–cpx cumul	0.805							0.13		
8–44	ol–cpx cumul										

Data are from Ionov et al. (2005c,e); collection year is omitted in sample numbers (e.g., 1–2 instead of 9501-2). ol, olivine; opx, orthopyroxene; cpx, clinopyroxene; spl, spinel; fs, feldspar; phl, phlogopite; am, amphibole; ap, apatite; (am, phl), minerals replaced by fine-grained fs-bearing material; crypt., cryptocrystalline interstitial material; tr., trace amounts. Samples with $\geqslant 0.06\%$ P_2O_5 are assumed to contain apatite. Mg#, $Mg/(Mg + Fe)_{at}$ and Cr#, $Cr/(Cr + Al)_{at}$. *T* estimates are after Brey and Köhler (1990).

(Table 1). (1) The predominant lherzolite–harzburgite (LH) series groups "normal" (in terms of Mg# and modal compositions) fertile to refractory rocks (the latter are most common), which can be considered residues of shallow partial melting (Ionov et al., 2005e). (2) Subordinate lherzolite–wehrlite (LW) series rocks have low Mg# (0.84–0.89), high modal olivine (66–84%) and high cpx/opx; they were produced by reaction of evolved under-saturated silicate melts with refractory partial melting residues, which caused replacement of opx by cpx and Fe-enrichments (Io-

nov et al., 2005c). (3) Olivine–cpx cumulates have a broad range of modal compositions and low Mg# (⩽0.84).

We refer to Ionov et al. (2005c,e) for petrographic and major element data on those xenoliths. Here, we consider in detail textural position and compositions of (1) composite cpx and (2) accessory metasomatic hosts of incompatible elements (phosphates, alkali feldspar, and Ba–Ti-rich micas), which were not fully addressed in the earlier work.

3.1. Clinopyroxene generations

Ionov et al. (2005e) found unusually broad Na_2O ranges in cpx from three LH xenoliths and suggested that cpx populations with distinct compositions may exist in those samples. Here, we identify at least three generations of coarse cpx in xenolith 10–19 (Fig. 1A and Table 2). Cpx-1 (~1.8% Na_2O) makes up relatively large equant grains. Cpx-2 (~0.7% Na_2O) usually mantles cpx-1 (Fig. 1A). Cpx-3 (~2.7% Na_2O) is least common; it mainly occurs next to opx and may replace the latter. While cpx-1 must have formed earlier than cpx-2 and cpx-3 based on textural relationships, it cannot be considered a "pre-metasomatic" phase formed by partial melting because it has too much Na_2O for a residual cpx in a refractory peridotite (Takazawa et al., 2000; Hellebrand and Snow, 2003; Ionov et al., 2005e). Furthermore, cpx-1 hosts abundant empty vugs and fluid micro-inclusions (Fig. 1A) and hence crystallised in a fluid-rich environment. Small phosphate grains locally

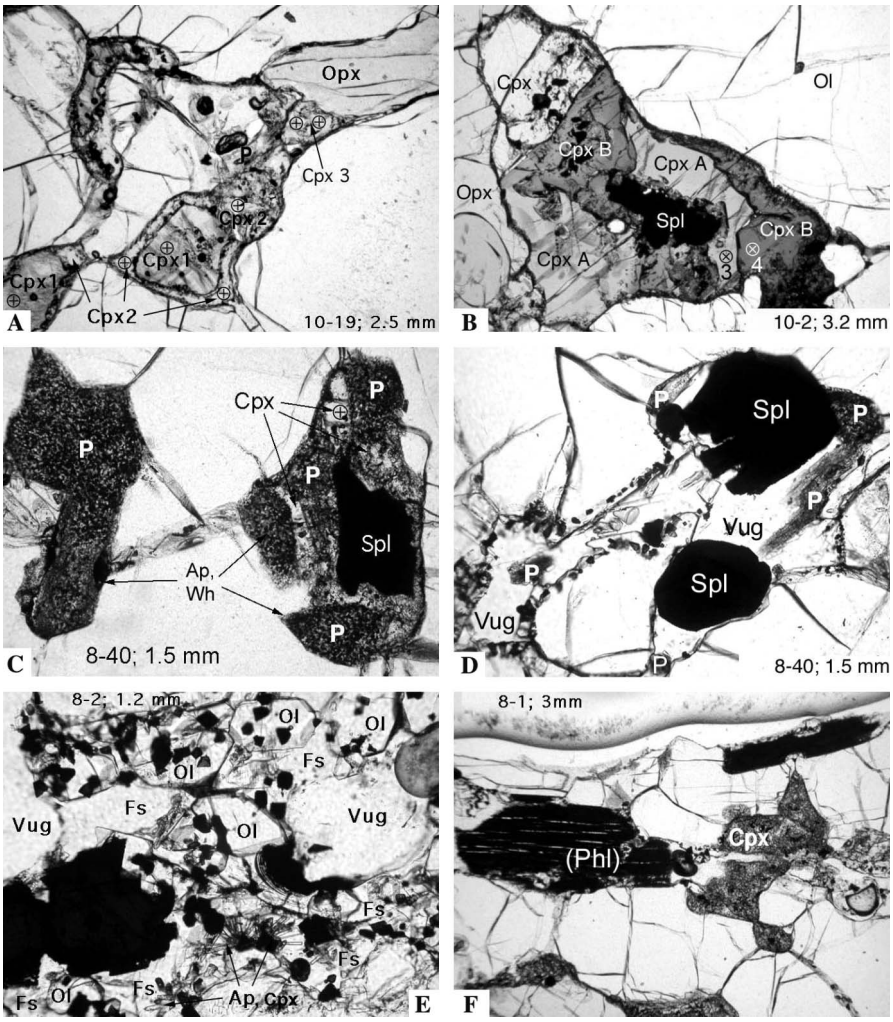

Fig. 1. Photomicrographs of metasomatised Tok peridotite xenoliths (LH series) in plane-polarised transmitted light. Sample numbers and the field of view along the long axis are shown on the photos. Cpx, clinopyroxene; Opx, orthopyroxene; Ol, olivine; Spl, spinel; Fs, feldspar; P, phosphate; Ap, apatite; Wh, whitlockite; Phl, phlogopite. Circled crosses show EPMA and SIMS spots. (A) Three generations of cpx with distinct Na_2O (0.7–2.7%). Average EPMA for each generation are given in Table 2. Cpx 3 may have replaced opx. Note a small phosphate aggregate in the centre. (B) Composite cpx aggregates around spinel. Cpx-A and cpx-B have distinct Na_2O (3% vs. 1.6%; Table 3) and can be distinguished optically by pleochroism colours. Numbers 3 and 4 next to circled crosses in cpx-A and cpx-B indicate spots of corresponding EPMA and SIMS analyses given in Table 3. (C) Spongy aggregates of apatite and whitlockite. Cpx intergrown with the phosphates has moderate Na_2O (1.2%, Table 1). (D) An empty cavity (vug) lined with fine-grained ol and spl contains phosphate grains (e.g., subhedral apatite at the top) and spongy ap–wh–fs aggregates (top right corner; same as in Fig. 2D). (E) Fine-grained aggregate of late-stage ol, spl, fs and phosphates with empty vugs. Large dark grain is resorbed primary spinel. (F) Decayed phl grains (dark, with relict cleavage) and spongy cpx.

Table 2
EPMA (in wt.%) for metasomatic minerals in Figs. 1 and 2

Sa. No.:	10–19			8–40												
Miner.:	Clinopyroxene (aver.)			Clinopyroxene				opx	Feldspar		spl	Phosphates		Phl breakdown products			
Type:	cpx-1	cpx-2	cpx-3	at ap	at op	spongy	2nd	2nd	host	vein	pool	2nd	whitl.	ap	Ba-phl	Ba-phl	fs	ol
Fig. No.:	1A	1A	1A	1C		2A	2B	2C	2B	2B	2C	2C	2C	2D	2E	2E	2E	2E
SiO_2	53.42	52.61	53.06	52.05	53.06	52.82	54.05	52.01	55.56	68.86	60.80	0.42	0.14	0.21	31.11	31.05	57.74	39.32
TiO_2	0.16	0.07	0.17	0.09	0.10	0.10	0.13	0.54	0.02	0.30	0.88	1.46	0.00	0.01	13.40	14.34	0.78	0.08
Al_2O_3	3.11	2.78	5.16	3.36	4.85	2.49	0.51	2.78	1.82	17.55	24.24	35.00	0.00	0.00	21.50	17.00	26.87	1.11
Cr_2O_3	0.98	1.43	1.94	2.99	2.75	2.56	1.66	1.85	0.60	0.01	0.02	32.01	0.08	0.00	3.10	1.19	0.09	0.87
FeO	2.74	2.80	2.65	2.53	2.60	2.86	2.45	2.18	5.71	0.84	0.56	12.59	0.36	0.10	5.10	5.13	0.38	7.64
MnO	0.11	0.10	0.10	0.09	0.10	0.09	0.09	0.10	0.18	0.03	0.00	0.20	0.00	0.00	0.04	0.03	0.01	0.11
MgO	16.73	19.28	15.24	17.27	15.01	17.22	18.55	17.19	34.71	0.42	0.25	17.58	3.50	0.19	12.58	13.19	0.14	51.08
CaO	19.60	19.20	17.97	19.96	17.58	20.16	21.11	21.89	0.64	0.06	0.18	0.01	43.89	51.26	0.09	0.05	0.50	0.10
Na_2O	1.81	0.68	2.68	1.16	2.91	1.35	0.77	0.70	0.16	2.54	1.90	0.01	2.30	0.14	1.26	0.66	5.23	0.04
K_2O	nd	nd	nd	0.01	0.01	0.01	0.01	0.04	0.00	6.19	5.81	0.01	0.12	0.00	4.90	4.15	0.50	0.01
NiO	0.05	0.09	0.04	0.11	0.05	0.05	0.05	0.10	0.10	0.00	0.00	0.25	0.02	0.00	0.21	0.24	0.04	0.39
P_2O_5	nd	nd	nd	0.08	0.07	0.04	0.06	0.06	0.05	0.36	0.37	0.00	51.25	46.78	0.10	0.04	0.36	0.02
BaO	nd	nd	nd	0.00	nd	nd	nd	nd	nd	nd	nd	nd	nd	nd	7.44	12.22	0.07	0.04
Total	98.7	99.0	99.0	99.7	99.1	99.8	99.4	99.4	99.6	97.2	95.0	99.5	101.7	98.7	100.8	99.3	92.7	100.8
Mg#	0.916	0.925	0.911	0.924	0.911	0.915	0.931	0.934	0.915			0.71			0.81	0.82		0.923

nd, not determined. Whitl, whitlockite; other symbols are as in Table 1.

occur close to cpx-2 and cpx-3 (Fig. 1A) but it is not clear from the textural evidence if those minerals formed simultaneously. Overall, all these cpx generations appear to be of metasomatic origin.

Two types of cpx can be distinguished optically in coarse cpx aggregates around spinel in xenolith 10–2 (cpx-A and cpx-B, Fig. 1B). Cpx-A contains nearly twice as much Na_2O as cpx-B (~3.0% vs. 1.6%) as well as more Al and less Ti (Table 3). Cpx-B may locally replace cpx-A but they are usually intergrown. In general, the number of cpx types, their compositions (Na–Al–Cr–Ti; Tables 2 and 3) and textural relationships in the Tok xenoliths are not uniform. The only apparent similarity between the cpx populations in different samples is that they all include a Na-rich variety (2.5–3.0% Na_2O). This Na-rich cpx is not likely to have been formed in the most recent metasomatic episode or be related to late-stage accessory minerals. For example, cpx grains intergrown with spongy phosphates in sample 8–40 (Fig. 1C) contain much less Na_2O than those adjacent to opx (~1.2% vs. 3.0%, Table 2); interstitial phosphates in xenolith 10–19 appear to be spatially associated with Na-poor cpx-2 (~0.7% Na_2O).

3.2. Accessory metasomatic phases

Inter-granular materials of metasomatic origin, in particular, alkali-rich feldspars, are common in olivine-rich Tok peridotites. As shown by Ionov et al. (1995a, 1999) metasomatic feldspar in peridotite xenoliths from southern Siberia and other regions has broad Ca–Na–K variations but is typically alkali-rich with common high K, and is thus distinct from Ca-rich plagioclase in orogenic peridotites. The feldspar forms interstitial veins and pools, which also contain late-stage cpx, olivine, spinel and phosphates (Figs. 1E, 2B and C and Table 2). The alkali feldspar typically contains much Fe, Mg and Ti and is hard to distinguish from Mg-poor, K–Na–Al–rich silicate glass based on microscopic and EPMA data alone; these phases were identified using Raman micro-spectroscopy. Silicate glass is rare and mainly occurs in vermicular micro-channels in spongy cpx (Fig. 2A). Relatively low totals of feldspar EPMA in Table 2 are mainly related to rapid loss of alkalis during analyses with focused beam employed to analyse small targets (EPMA spots are seen in Figs. 2B and C). Beam sizes of $\geqslant$8–10 μm are required to obtain high-quality feldspar and glass analyses.

Two phosphate mineral species have been identified in the Tok xenoliths, apatite and whitlockite. Whitlockite (http://www.mindat.org/min-4280.html) is an "anhydrous", halogen-free phosphate [$(Ca,Mg)_3(PO_4)_2$ or $Ca_9(Mg,Fe^{2+})(PO_4)_7$]. It is common in meteorites and lunar rocks, but had not been reported in terrestrial mantle-derived rocks before its recent discovery in the Tok xenoliths (Ionov et al., 2005d). The Raman spectrum of whitlockite contains a hump with peaks at 959 and 975 cm^{-1} while apatite has a single peak at 961 cm^{-1}. Whitlockite in the Tok xenoliths has 2–4% Na_2O and

Table 3
EPMA (wt.%) and SIMS (ppm) data for adjacent low-Na and high-Na cpx in sample 10–2

	Cpx-A (high-Na)					Cpx-B (low-Na)				
An. No.:	1	3	5	Aver.	1σ/mean (%)	2	4	6	Aver.	1σ/mean (%)
EPMA (wt.%)										
SiO_2	54.20	54.54	54.29	54.34	0.3	52.99	53.16	53.38	53.17	0.4
TiO_2	0.08	0.07	0.08	0.08	4	0.25	0.14	0.12	0.17	39
Al_2O_3	4.51	4.41	4.52	4.48	1	3.73	3.37	3.20	3.43	8
Cr_2O_3	2.45	2.72	2.61	2.59	5	2.42	2.79	2.85	2.69	9
FeO	2.31	2.31	2.38	2.33	2	2.33	2.54	2.62	2.49	6
MnO	0.11	0.07	0.08	0.08	24	0.12	0.10	0.11	0.11	11
MgO	15.23	15.08	15.29	15.20	1	16.86	17.11	17.38	17.12	2
CaO	18.07	17.87	17.73	17.89	1	19.14	19.03	18.68	18.95	1
Na_2O	2.99	2.99	2.97	2.98	0.3	1.66	1.56	1.66	1.62	3
Total	99.9	100.1	99.9	100.0		99.5	99.8	100.0	99.8	
SIMS analyses (ppm)										
Ti	557	469	534	520	9	1105	710	611	809	32
V	nd	278	266	272	3	284	266	243	264	8
Sr	382	549	399	443	21	247	246	217	236	7
Y	26.2	21.0	26.6	24.6	13	21.4	21.5	26.5	23.1	13
Zr	199	26.4	109	111	78	42.5	53.9	99.1	65.1	46
Nb	1.31	1.12	1.26	1.23	8	1.02	0.61	0.56	0.73	35
La	8.72	10.6	8.78	9.4	11	4.90	5.97	5.01	5.29	11
Ce	32.6	37.0	33.3	34.3	7	23.1	26.7	22.8	24.2	9
Nd	30.4	32.4	32.5	31.8	4	27.9	30.3	28.6	28.9	4
Sm	8.72	7.75	8.86	8.44	7	7.80	7.79	8.29	7.96	4
Eu	2.81	2.50	3.01	2.77	9	2.53	2.57	2.81	2.63	6
Tb	1.13	0.84	1.12	1.03	16	0.87	0.89	1.09	0.95	13
Gd	7.78	5.98	7.78	7.18	14	6.41	6.41	7.67	6.83	11
Dy	5.38	4.20	5.80	5.13	16	4.60	4.56	5.70	4.95	13
Er	2.38	1.96	2.47	2.27	12	1.78	1.94	2.50	2.07	18
Yb	1.52	1.34	1.69	1.52	11	1.31	1.20	1.49	1.34	11
Hf	3.20	0.29	1.08	1.52	99	0.58	0.93	1.88	1.13	60
Th	0.14	0.13	0.11	0.12	13	0.04	0.01	0.09	0.05	79
Zr/Hf	62	92	100	85	24	73	58	53	61	17
Ti/Zr	3	18	5	8	95	26	13	6	15	67

See Fig. 1B for sites of analyses No. 3 and 4; nd, not determined.

MgO, with Cl and F below detection limits; it also contains more FeO, K_2O and P_2O_5 and less CaO than apatite (Table 2).

Small (<30 μm) prismatic or anhedral grains of apatite and whitlockite occur in interstitial veins and pockets, usually in association with feldspar and late-stage cpx, olivine and spinel (Figs. 1E and 2B and C). Phosphates are also common in empty vugs; they range from subhedral crystals to spongy aggregates (Fig. 1D). High-resolution back-scattered electron (BSE) images show that some phosphate grains are complex, vermicular intergrowths of apatite with minor alkali feldspar on a micrometer-scale (Fig. 2D). Some of those grains protrude into the vugs and look "suspended" (Figs. 1D and 2D) indicating that they may have crystallised from hypothetical fluids that once filled the vugs. Several xenoliths, in particular 8–40, contain fairly large (up to 1 mm) and abundant spongy apatite–whitlockite aggregates (Fig. 1C).

Some Tok xenoliths (Table 1) contain accessory amphibole (amph) and phlogopite (phl) (Ionov et al., 2005c,e). In many cases, these minerals are completely or partially replaced by fine-grained aggregates of feldspar, olivine, cpx and oxide minerals (Figs. 1F and 2F). We emphasize that no silicate glass was found in the replacement products, which are fully crystalline and cannot have formed by melting due to rapid heating and decompression during the transport of the xenoliths to the surface. Such aggregates were earlier found in xenoliths from other localities in southern Siberia (southern Baikal region, Sikhote-Alin) and attributed to a specific type of mantle metasomatism related to water-poor fluids (Ionov et al., 1999; Kalfoun et al., 2002).

Two features of this phenomenon in the Tok xenoliths are of particular interest. First, no unaltered amph and phl were found in rocks that contain whitlockite (Figs. 1C and D). Hence, it is possible that it was reaction with the fluid, which precipitated the phosphates that triggered the breakdown of amph and phl. The latter process also appears to be linked with replacement of clear cpx grains with spongy or fine-grained cpx (Fig. 1F). Second, the phl breakdown products in some xenoliths contain a Ba–Ti-rich silicate (Fig. 2E and Table 2), which has not been reported from other mantle peridotites and might be a water-poor mica species. It forms very small (<20 μm) pris-

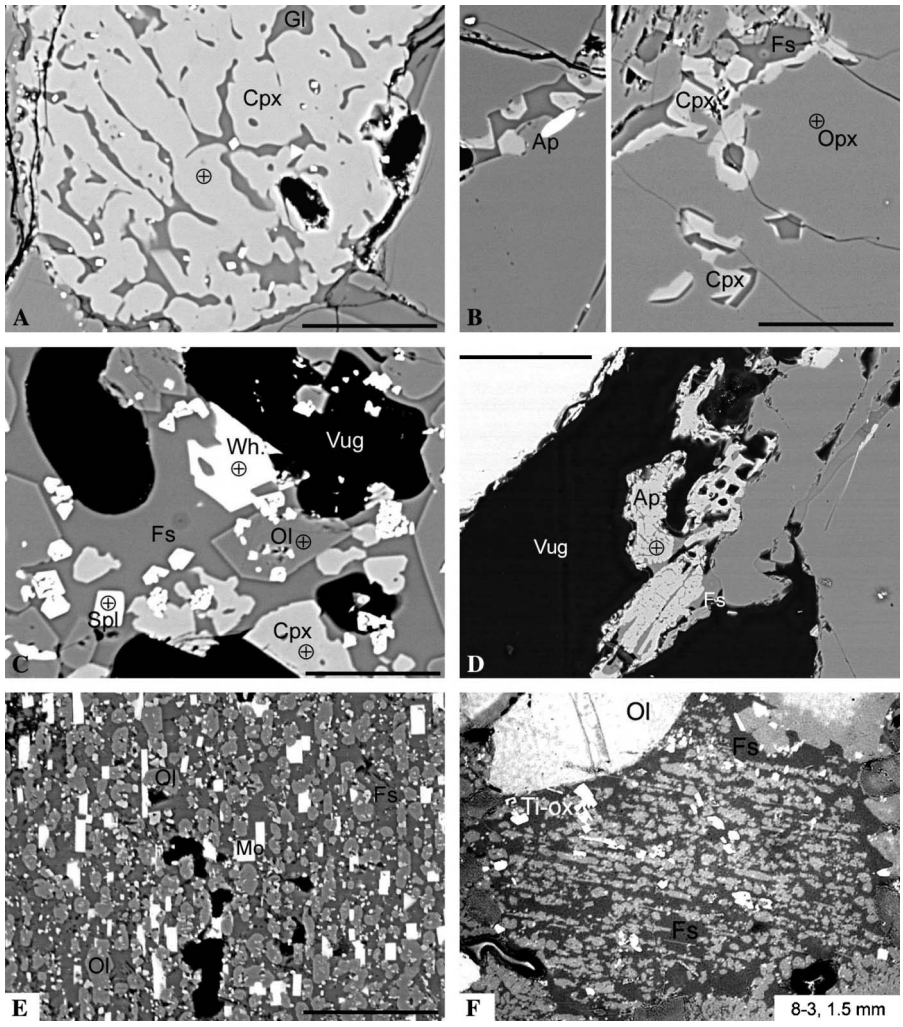

Fig. 2. BSE images of metasomatic features in xenolith 8–40. Symbols are same as in Fig. 1. EPMA for spots marked with circled crosses are given in Table 2. (A) Micro-channels in spongy cpx are filled with Na–Al-rich silicate glass (Gl) with rare euhedral spinel. Scale bar is 50 μm. (B) Two sections of an inter-granular feldspar vein containing euhedral cpx and rare phosphates (bright). Opx next to the vein has fs–cpx inclusions or channels. Scale bar is 50 μm. (C) Interstitial pocket (connected with the vein in B) of late-stage cpx, ol, spl and phosphates in alkali feldspar matrix with empty vugs. Scale bar is 50 μm. (D) A detail of central right Fig. 1D showing spongy, vermicular apatite intergrown with feldspar protruding into an empty vug. Scale bar is 100 μm. (E) Inner part of a decayed phl grain (similar to that in Fig. 1F) replaced by an aggregate of alkali feldspar (dark) with equant to euhedral grains of ol, spl and Ba–Ti-rich silicate (bright). The latter is provisionally referred to here as montpellierite (Mo) after the place where it was first found by EPMA. Prismatic Mo and elongated ol grains are aligned parallel to the cleavage of the predecessor phl. Scale bar is 50 μm. (F) Reflected-light photomicrograph of decayed amph in xenolith 8–3 replaced by alkali feldspar (dark matrix), ol, cpx, spl and Ti-rich oxides (bright; mainly ilmenite and rare armalcolite).

matic grains oriented parallel to each other and to elongated late-stage olivine (possibly along the cleavage of the predecessor mineral), with hexagonal sections perpendicular to the long axis. It has arguably the highest contents of BaO (12%) and TiO_2 (15%) among silicate minerals in peridotite massifs and basalt-hosted mantle xenoliths.

4. Trace element compositions

4.1. Clinopyroxene

LA-ICPMS analyses of pyroxenes are given in Table 4. Cpx in fertile (15–17% cpx) LH series rocks has nearly flat REE patterns and a narrow range of primitive mantle-normalised abundances ($REE_{PM} = 3–5$; Fig. 3A). In detail, these patterns are spoon-shaped, such that the REE_{PM} decrease from Eu to Nd and have La–Ce "inflections". Cpx in LH series lherzolites with lower modal cpx (6–14%) is LREE-enriched ($La/Nd_{PM} > 1$; $Nd/Yb_{PM} > 1$; Fig. 3C). The cpx patterns change in concert with modal compositions, e.g., abundances of light and middle REE and Sr are negatively correlated with modal cpx while HREE are similar (Figs. 3C and D).

Cpx in nearly all olivine-rich peridotites (both LH and LW series) has convex-upward REE patterns ($La/Nd_{PM} < 1$; $Nd/Yb_{PM} \gg 1$; Figs. 3E and G) with a much more narrow LREE–MREE variation range than for cpx from LH series lherzolites. HREE abundances in the cpx

Table 4
LA-ICPMS analyses (in ppm) of minerals and reference materials

	BCR-2G		BCR-2			Clinopyroxene													
	This work		Norman	Eggins	Raczek	1–2	1–3	1–13	2–1	2–2	2–3	2–4	2–6	2–9	2–10	3–2	3–4	3–19	3–22	5–3
	av. 12	RSD (%)				av. 2	av. 2	av. 2	av. 3	av. 3	av. 3	av. 3	av. 2	av. 2	av. 2	av. 2	av. 2	av. 2	av. 2	av. 2
Sc	34.8	5	33	34		137	111	103	45				86	87	60	63	94	75	62	78
Ti	16,280	8	13,730	13,803		137	639	1242	2710	1722	1150	1080	903	767	2325	1037	1550	781	1540	534
V	444	4	414	427		425	431	332	151				231	300	223	120	271	221	204	270
Ni	12	5	10.8			317	364	351	381											
Rb	48	7	49	46.1	46.9	0.24	0.54	0.20	0.10		0.36	0.08	0.10	0.11	<0.06	0.08	0.84	0.07	<0.07	<0.06
Sr	317	2	342	338	340	475	431	399	258	241	302	448	400	569	255	447	218	687	336	527
Y	30.4	4	35.3	36.2		14.7	30.6	24.1	30.3	15.5	24.7	24.2	12.3	18.9	18.7	20.1	31.4	9.1	19.1	6.1
Zr	156	4	194	192		71.7	75.4	121	148	27.6	13.6	66.6	51.6	19.9	77.3	131	131	62.2	172	1.9
Nb	12.5	4	12.8	12.8		0.52	2.30	2.31	1.56	0.53	0.76	0.88	0.69	0.84	1.27	0.85	2.10	0.34	1.05	0.37
Ba	634	3	660	662	677	0.3	2.0	1.0	0.4	0.3	0.3	0.7	0.3	3.6	0.7	0.8	9.3	0.7	0.2	0.5
La	24	4	24.5	24.6	24.9	7.9	9.5	11.1	6.5	6.8	11.1	11.8	13.4	15.0	7.2	9.7	7.1	16.6	7.2	17.4
Ce	50.3	3	50.5	50.4	52.9	31.2	39.1	39.4	25.3	24.6	44.0	41.2	39.3	49.5	26.8	31.1	28.4	40.6	27.8	29.0
Pr	6.3	5	6.8		6.57	5.5	7.3	6.5	4.9	3.9	6.8	6.1	5.3	7.3	4.7	5.3	5.2	5.1	4.9	2.6
Nd	26.3	4	29	26.8	28.7	26.6	38.0	31.3	27.5	19.9	33.5	29.1	22.2	33.4	23.8	27.1	28.5	19.5	25.7	7.6
Sm	6.2	4	6.6	6.41	6.57	7.2	10.7	8.2	8.6	5.1	8.0	7.2	4.5	7.7	6.0	7.6	8.8	3.5	7.0	0.8
Eu	1.9	4	1.9	1.91	1.96	2.3	3.6	2.7	2.9	1.6	2.7	2.4	1.5	2.4	1.9	2.5	2.7	1.04	2.3	0.35
Gd	6.2	4	6.5	6.44	6.75	5.5	8.8	7.2	8.2	4.4	6.9	6.3	3.7	6.2	4.9	6.7	8.4	2.3	6.5	0.7
Tb	0.90	5	1.06		1.07	0.76	1.25	0.99	1.23	0.58	0.93	0.85	0.49	0.77	0.68	0.92	1.16	0.30	0.86	0.11
Dy	6.0	3	6.5	6.18	6.41	3.75	7.10	5.60	7.07	3.26	5.10	4.90	2.60	4.30	4.05	5.05	6.90	1.72	4.70	0.91
Ho	1.2	5	1.32		1.3	0.58	1.20	0.96	1.24	0.56	0.89	0.85	0.46	0.74	0.76	0.81	1.25	0.34	0.78	0.23
Er	3.3	5	3.6	3.60	3.66	1.30	3.00	2.35	3.07	1.44	2.22	2.16	1.17	1.87	1.96	1.93	3.10	0.91	1.84	0.76
Tm	0.47	3				0.15	0.38	0.30	0.39	0.19	0.27	0.29	0.16	0.25	0.28	0.25	0.39	0.12	0.22	0.13
Yb	3.2	6	3.5	3.32	3.38	0.82	2.15	1.71	2.33	1.14	1.72	1.75	0.96	1.51	1.78	1.37	2.35	0.86	1.33	0.88
Lu	0.46	5	0.51	0.50	0.52	0.11	0.30	0.23	0.32	0.16	0.22	0.24	0.14	0.19	0.24	0.20	0.32	0.13	0.17	0.14
Hf	4.4	7	5.0	4.74		0.84	1.25	1.58	3.13	0.42	0.28	1.16	0.85	0.18	1.40	1.87	3.85	1.80	3.45	<0.02
Ta	0.78	3	0.78	0.77		0.02	0.10	0.30	0.17	0.052	0.044	0.066	0.13	0.047	0.23	0.09	0.17	0.01	0.12	0.017
Pb	11.4	12	11.5	10.3		0.4	0.3	0.6	0.4	1.2	0.3	0.6	0.4	0.8	0.4	1.6		2.4	0.4	1.2
Th	5.62	5	6.1	5.72		0.11	0.21	0.35	0.19	0.32	0.24	0.32	0.25	0.78	0.31	0.26	0.13	0.71	0.09	0.92
U	1.74	5	1.73	1.58		0.051	0.085	0.11	0.065	0.086	0.081	0.093	0.048	0.17	0.10	0.065	0.035	0.16	0.024	0.15

	Clinopyroxene																			
	6–0[a]		6–1	6–2	6–3	7–1	7–5	8–1	8–2	8–3	8–5	8–6	8–7	8–8	8–10	8–11	8–14[a]	8–31	8–39	8–40[a]
	cpx-1	cpx-2	av. 2	av. 2	av. 2	av. 2	av. 2	av. 2	av. 2	av. 2	av. 2	av. 2	av. 2	av. 2	av. 3	av. 3		av. 3	av. 2	av. 3
Sc			62	65	60	96	65	77	85	113	62	76	123	107	65	80		84	56	
Ti	684	160	3889	4013	614	1114	2733	1506	832	2382	1946	3430	284	1478	1867	1573	6927	522	3488	558
V			290	305	272	429	291	276	407	449	277	266	341	370	376	552		329	282	
Ni															7	5		7		323
Rb	1.40	0.20	<0.09	<0.14	0.16	0.53	<0.13	0.28	0.84	3.35	0.47	<0.2	0.90	1.12	1.09	0.7	0.004	1.32	<0.2	0.014
Sr	659	966	87	87	85	348	112	281	404	399	247	90	513	542	246	344	96	488	73	746
Y	13.5	13.2	17.2	17.6	5.9	26.8	15.9	11.6	14.3	28.2	14.0	17.3	17.9	20.6	25.6	24.1	11.4	27.2	16.3	11.1
Zr	22.5	36.1	33.2	33.7	5.7	129	22.6	55.8	92.8	139	117	34.1	189	194	63.5	120	30.5	71.5	34	30.5
Nb	1.79	0.20	0.43	0.45	1.64	2.28	0.51	1.30	1.65	1.24	2.00	0.54	1.61	2.15	1.06	2.39	0.28	4.53	0.49	0.35
Ba	3.9	13	0.4	0.3	0.2	0.6	0.5	1.3	0.8	18	0.4	0.1	1.2	2.7	2.5	0.3	0.07	9.7	0.1	5.9
La	31.4	24.6	2.4	2.1	4.2	9.7	5.6	10.6	13.8	15.6	8.0	2.9	12.9	14.4	9.6	10.0	2.17	15.3	2.5	17.9
Ce	66.2	51.4	5.8	5.2	8.4	30.1	11.2	30.2	40.5	39.3	23.4	6.6	40.5	41.4	3.2	30.1	7.96	43.9	5.6	54.6

Pr	8.11	6.79	0.97	0.92	1.07	5.8	1.5	5.1	6.6	7.1	4.2	0.92	7.5	7.4	5.4	6.0	1.53	7.9	0.80	7.56
Nd	30.0	27.0	4.6	4.6	3.5	28.9	6.1	21.9	25.8	32.4	18.0	4.8	33.7	31.7	23.6	27.4	8.56	35.2	4.3	31.2
Sm	5.12	4.86	1.9	1.8	0.7	9.1	1.9	4.8	5.8	8.9	4.1	1.8	8.6	8.5	7.8	8.2	2.82	9.7	1.9	4.98
Eu	2.10	1.61	0.72	0.75	0.22	3.0	0.64	1.3	1.7	2.9	1.2	0.69	2.4	2.6	2.5	2.8	1.06	3.3	0.70	1.51
Gd	4.06	3.62	2.5	2.6	0.7	8.2	2.1	3.4	4.0	7.8	3.0	2.4	5.6	6.5	6.6	7.1	2.95	8.7	2.4	3.38
Tb	0.50	0.48	0.44	0.47	0.12	1.18	0.40	0.44	0.55	1.13	0.45	0.42	0.74	0.90	1.08	1.09	0.44	1.30	0.49	0.42
Dy	2.73	2.75	3.10	3.05	0.91	6.30	2.95	2.45	2.90	6.05	2.65	3.70	3.60	4.30	5.55	5.67	2.67	6.73	3.50	2.24
Ho	0.49	0.47	0.66	0.72	0.22	1.10	0.64	0.48	0.53	1.10	0.54	0.71	0.65	0.77	1.04	0.99	0.48	1.16	0.68	0.38
Er	1.24	1.14	1.92	1.98	0.73	2.54	1.85	1.18	1.37	2.65	1.48	2.15	1.50	1.83	2.53	2.35	1.22	2.65	2.10	0.98
Tm	0.17	0.16	0.29	0.28	0.12	0.32	0.26	0.18	0.21	0.32	0.21	0.37	0.20	0.25	0.36	0.30	0.15	0.34	0.29	0.13
Yb	1.07	1.03	1.66	1.71	0.72	1.67	1.71	1.08	1.19	1.83	1.31	2.25	1.22	1.26	1.82	1.63	0.93	1.85	2.15	0.87
Lu	0.15	0.14	0.25	0.26	0.14	0.24	0.22	0.16	0.20	0.26	0.21	0.26	0.20	0.21	0.32	0.24	0.12	0.26	0.29	0.13
Hf	0.50	0.32	1.02	1.06	0.15	2.25	0.75	1.36	0.98	2.86	2.05	1.10	2.15	2.00	1.35	1.73	1.30	1.82	1.15	0.81
Ta	0.062	0.017	0.03	0.03	0.09	0.32	0.02	0.21	0.32	0.17	0.27	<0.03	0.22	0.34	0.10	0.33	0.044	0.12	<0.05	0.023
Pb	0.98	1.32	0.2	0.3	0.3	0.4	0.3	0.4	0.4		0.3	<0.23	0.5	0.8	0.5	0.5	0.03	0.64	0.40	0.72
Th	0.86	1.13	0.12	0.14	0.25	0.22	0.55	0.35	0.41	0.46	0.43	0.42	0.25	0.40	0.40	0.27	0.033	0.26	0.62	0.16
U	0.13	0.12	0.034	0.047	0.063	0.074	0.13	0.095	0.13	0.13	0.12	0.12	0.084	0.11	0.13	0.091	0.009	0.090	0.23	0.05
	Clinopyroxene												am	phl	/phl/	Orthopyroxene				
	8–50	10–1	10–2		10–3	10–4	10–8	10–11	10–16	10–17	10–19		2–3	3–2	8–1	1–13	2–2	2–3	2–6	2–9
	av. 4	av. 3	cpx-1	cpx-2	av. 2	av. 2	av. 2	av. 2	av. 2	av. 2	cpx-1	cpx-2								
Sc														9	47	10	10	9	14	14
Ti			605	2966	3450	524	1320	2043	2456	3930	1040	1575	92,700	44,230	50,880	90	133	12	343	103
V			352	299	160	175	361	218	313	262	211	349		315	1240	38	42	40	68	45
Ni																571	676	646		
Rb	<0.06	0.08	<1.5	<1.7	<0.5	<0.5	<0.7	<0.5	<1	<0.7	<1.3	<0.7	0.96	125	59	<0.05	<0.04	<0.07	<0.04	<0.04
Sr	219	146	744	227	373	332	431	210	497	228	252	818	1600	314	1537	2.04	0.80	2.08	0.67	0.50
Y	10.8	16.2	14	20.8	23.1	21.5	17.7	20.6	13.6	16.0	6.3	10.9	4.4	0.45	12.6	0.75	0.71	0.66	0.80	0.74
Zr	82.7	33.6	21.6	62.7	201	162	110	73	121	69.5	50.9	69.2	54.8	16.6	125	2.30	1.23	0.49	3.00	0.28
Nb	1.46	0.64	0.7	2.3	0.90	1.25	1.50	1.00	1.10	1.55	1.00	2.80	56.9	57.0	188	0.07	0.03	0.05	0.07	0.05
Ba	0.3	0.1	1.6	5.1	0.2	0.3	0.3	7.1	0.2	0.2	0.2	4.2	3710	2510	32300	<0.024	0.21	0.25	<0.010	<0.012
La	8.0	4.8	16.1	5.3	9.4	9.1	10.7	7.4	11.8	10.9	11.6	24.5	11.1	<0.013	23.2	0.07	0.08	0.21	0.01	0.01
Ce	25.6	16.0	53.2	22.5	33.7	35.4	43.6	28.1	47.1	29.5	36.3	63.7	25.6	<0.011	55	0.25	0.14	0.30	0.08	0.06
Pr	3.8	2.5	7.8	4.4	5.7	6.3	7.8	5.2	7.3	3.9	5.0	8.8	2.8	<0.009	6.5	0.03	0.02	0.03	0.01	0.02
Nd	18.6	13.6	37.8	26.5	30.1	34.7	38.8	29.0	35.7	16.1	23.0	36.1	9.6	<0.14	24.9	0.24	0.11	<0.25	0.15	0.10
Sm	4.0	3.9	6.9	8.1	8.6	10.3	7.9	7.3	7.1	4.3	3.6	6.5	1.6	<0.08	3.7	<0.09	<0.07	<0.13	<0.08	0.07
Eu	1.1	1.4	2.4	2.6	2.9	3.2	2.7	2.6	2.2	1.4	0.90	2.0	2.0	0.06	2.5	0.04	<0.020	<0.04	0.03	0.02
Gd	3.1	3.8	5.3	7.1	8.6		7.1	8.3	5.8	4.1	1.7	4.2	2.9	0.46	20.9	<0.11	<0.09	<0.15	0.10	<0.06
Tb	0.40	0.58	0.8	1.1	1.20	1.30	1.00	1.20	0.65	0.70	0.30	0.60	0.14	<0.013	0.17	0.02	<0.013	<0.03	0.02	0.01
Dy	2.27	3.47	3.6	5.4	7.25	6.60	5.30	6.75	3.95	4.35	1.70	3.90	0.83	<0.05	1.3	0.14	0.11	<0.08	0.10	0.13
Ho	0.41	0.61	0.7	0.9	1.25	1.10	0.88	1.25	0.80	0.80	0.25	0.70	0.18	<0.013	0.23	0.03	0.02	0.03	0.04	0.03
Er	1.02	1.56	1.6	2.3	2.80	2.85	2.05	2.80	1.60	2.20	0.80	1.60	0.57	<0.04	0.6	0.09	0.10	0.09	0.09	0.10
Tm	0.14	0.20	0.2	0.4	0.45	0.31	0.24	0.30	0.21	0.34	0.23	0.26	0.12	<0.013	<0.10	0.02	0.02	0.03	0.02	0.02
Yb	0.82	1.25	1.5	1.6	2.30	2.00	1.85	2.15	1.30	2.10	0.70	1.50	0.66	<0.04	0.6	0.15	0.18	0.12	0.14	0.16
Lu	0.11	0.18	0.15	0.3	0.29	0.37	0.29	0.32	0.18	0.34	<0.11	0.20	0.09	0.02	<0.3	<0.024	0.02	<0.022	0.03	0.03
Hf	1.22	1.16	0.9	1.7	5.65	2.35	2.10	2.75	2.95	2.05	1.80	2.40	0.85	0.38	4.1	<0.06	<0.05	<0.11	<0.05	<0.03
Ta	0.15	0.086	<0,18	0.2	0.19	0.21	0.27	0.08	0.21	0.20	0.25	0.31	2	2.5	9.0	<0.022	<0.017	<0.03	<0.014	<0.010
Pb	0.3	0.4	2.3	<0.7	0.6	0.7	<0.4	0.4	0.5	1.1	0.9	3.1	1.5	2.9	5.9	<0.3	<0.19	<0.4	0.14	0.19
Th	0.39	0.32	0.5	<0.15	0.11	0.13	0.14	<0.05	0.27	0.53	0.19	0.90	0.50	<0.02	0.71	<0.04	0.02	<0.04	<0.012	<0.012
U	0.12	0.100	0.13	0.03	0.065	0.040	<0.05	0.050	0.090	0.15	0.100	0.20	0.19	0.02	0.20	<0.024	<0.017	<0.023	<0.009	<0.010

(*continued on next page*)

Table 4 (*continued*)

	Orthopyroxene																			
	3–4	3–19[a]	5–3[a]	6–0[a]	6–1[a] av. 2	6–2[a]	6–3[a]	7–1[a]	7–5[a]	8–1[a]	8–6	8–40[a]	10–2[a]	10–3[a]	10–4[a]	10–8[a]	10–11[a] av. 2	10–16[a]	10–17[a] av. 2	10–19[a] av. 2
Sc	12																			
Ti	262	248	144	162	1097	1113	187	533	760	644	722	310	295	553	224	250	154	307	882	430
V	66										89									
Ni		709	737		816	803	878	497	764	835		744	769	716	776	745	684	750	767	753
Rb	<0.05	0.002	0.001			0.003	0.001	0.005	0.000	0.002	<0.3		0.063				0.001			
Sr	0.43	1.44	0.10	0.46	0.26	0.30	0.03	5.10	0.21	0.34	0.39	1.34	0.89	1.25	0.85	1.01	1.11	1.21	0.61	0.54
Y	0.69	1.16	0.31	0.49	1.32	1.35	0.58	1.23	1.13	0.89	1.00	0.47	0.52	1.20	0.93	0.92	1.00	0.67	1.14	0.56
Zr	1.61	2.46	0.06	0.54	2.11	2.10	0.35	4.23	1.22	2.64	1.50	0.91	0.22	3.56	2.47	2.41	3.18	2.07	3.71	2.34
Nb	0.04	0.021	0.013	0.017	0.014	0.016	0.017	0.079	0.008	0.030	<0.25	0.02	0.037	0.036	0.034	0.044	0.021	0.027	0.050	0.046
Ba	0.10	0.14	0.00	0.00	0.01	0.02	0.03	0.01	0.00	0.00	<0.019	1.8	0.00	0.02	0.00	0.00	0.00	0.00	0.00	0.01
La	<0.013	0.067	0.014	0.020	0.006	0.006	0.002	0.113	0.008	0.019	<0.04	0.014	0.010	0.026	0.010	0.013	0.017	0.014	0.021	0.017
Ce	0.05	0.135	0.042	0.082	0.026	0.020	0.008	0.419	0.024	0.096	0.02	0.079	0.064	0.100	0.067	0.086	0.091	0.090	0.085	0.088
Pr	<0.010	0.021	0.005	0.014	0.005	0.005	0.001	0.078	0.004	0.021	<0.03	0.016	0.017	0.022	0.017	0.022	0.020	0.022	0.016	0.020
Nd	<0.12	0.127	0.024	0.065	0.045	0.036	0.011	0.475	0.025	0.156	<0.4	0.101	0.124	0.150	0.131	0.157	0.138	0.146	0.102	0.131
Sm	<0.10	0.058	0.007	0.024	0.027	0.029	0.004	0.163	0.017	0.053	<0.23	0.031	0.053	0.084	0.069	0.065	0.059	0.053	0.043	0.046
Eu	0.02	0.029	0.003	0.008	0.014	0.014	0.003	0.060	0.010	0.022	<0.04	0.012	0.023	0.035	0.031	0.030	0.026	0.025	0.021	0.016
Gd	0.07	0.106	0.012	0.027	0.065	0.063	0.017	0.195	0.046	0.073	<0.19	0.039	0.062	0.118	0.100	0.113	0.081	0.067	0.076	0.055
Tb	0.02	0.020	0.003	0.007	0.017	0.018	0.004	0.033	0.013	0.015	<0.04	0.007	0.010	0.025	0.021	0.020	0.017	0.014	0.018	0.010
Dy	0.07	0.175	0.030	0.058	0.169	0.176	0.060	0.235	0.127	0.127	0.20	0.064	0.071	0.189	0.158	0.155	0.145	0.106	0.160	0.082
Ho	0.02	0.041	0.011	0.016	0.047	0.050	0.019	0.047	0.040	0.032	004	0.016	0.015	0.045	0.036	0.034	0.035	0.023	0.041	0.019
Er	0.11	0.144	0.048	0.066	0.183	0.197	0.082	0.146	0.165	0.118	<0.09	0.049	0.061	0.146	0.114	0.110	0.128	0.081	0.156	0.072
Tm	0.03	0.025	0.010	0.012	0.035	0.036	0.018	0.022	0.032	0.024	0.06	0.010	0.012	0.027	0.019	0.018	0.023	0.013	0.029	0.013
Yb	0.20	0.217	0.118	0.114	0.303	0.317	0.170	0.152	0.291	0.191	0.17	0.085	0.095	0.212	0.148	0.143	0.191	0.116	0.251	0.114
Lu	0.03	0.038	0.019	0.018	0.054	0.060	0.028	0.024	0.052	0.035	0.11	0.017	0.019	0.031	0.022	0.026	0.032	0.021	0.043	0.020
Hf	<0.05	0.057	0.001	0.014	0.058	0.057	0.006	0.068	0.040	0.078	<0.09	0.035	0.006	0.049	0.032	0.052	0.035	0.034	0.087	0.069
Ta	<0.015	0.001	0.000	0.001	0.001	0.000	0.000	0.007	0.001	0.002	<0.05	0.002	0.001	0.002	0.002	0.003	0.001	0.001	0.001	0.003
Pb	<0.19	0.011	0.008	0.005	0.007	0.008	0.013	0.010	0.009	0.009	<0.4	0.010	0.008	0.015	0.009	0.006	0.007	0.009	0.010	0.012
Th	<0.023	0.029	0.012	0.004	0.001	0.006					<0.07	0.006	0.001	0.001	0.001	0.000	0.001	0.001	0.002	0.002
U	<0.014	0.003	0.003	0.005	0.001	0.001	0.001	0.003	0.002	0.003	<0.04	0.001	0.001	0.001	0.001	0.001	0.001	0.001	0.002	0.002

[a] Analyses done at MPI-Chemie, Mainz. BCR-2G values from this work are averages of 12 analyses (at Clermont-Ferrand). Other data for BCR-2 are from Norman (1998), Eggins (2003) and Raczek et al. (2001). Representative individual analyses are shown for cpx 6–0, 10–2 and 10–19; averages for 2–4 grains are given for other cpx;/phl/phlogopite breakdown products. Empty entries—not determined or failed determinations.

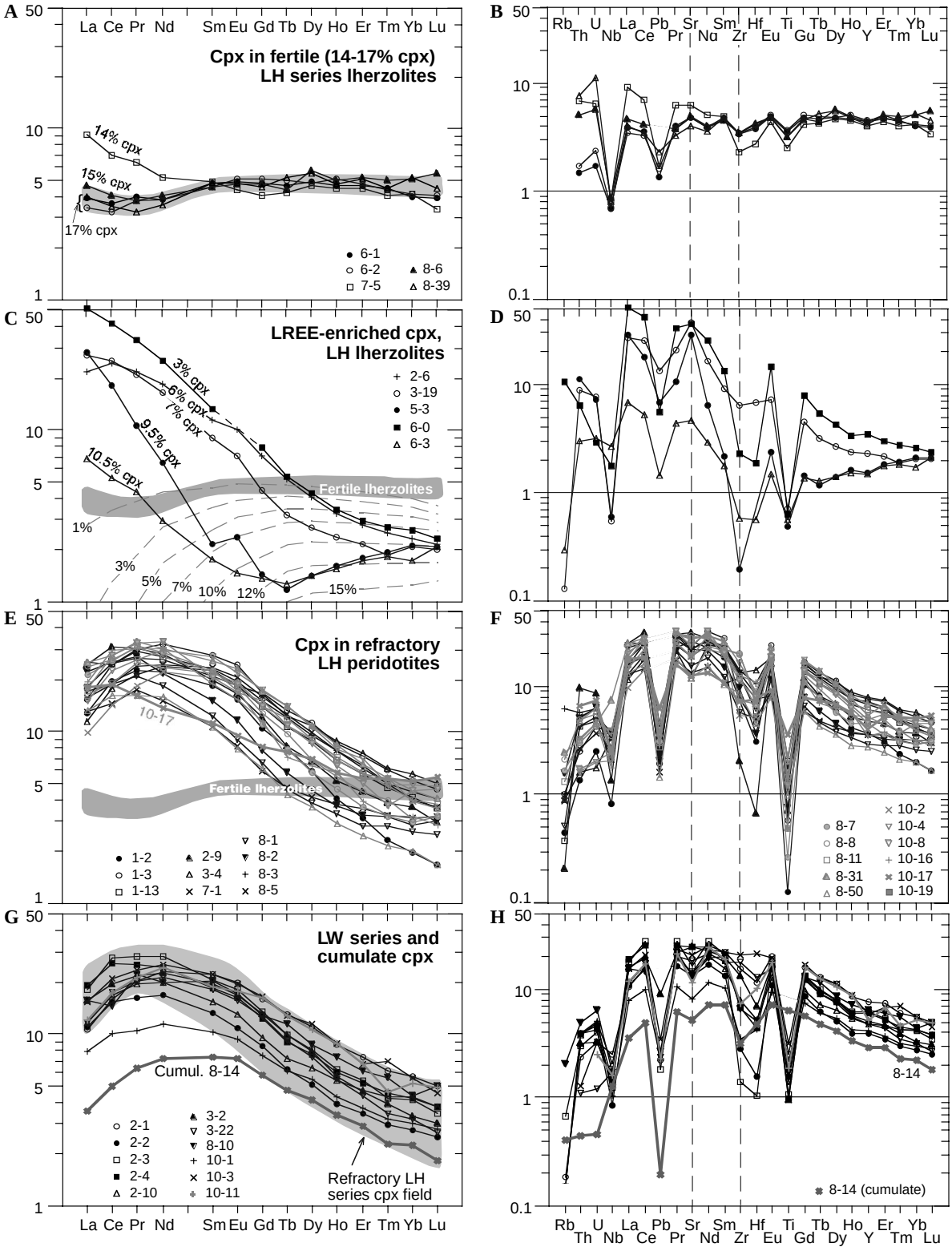

Fig. 3. (A–H) Primitive mantle-normalised (Hofmann, 1988) REE (left column) and multi-element abundance patterns of cpx in Tok xenoliths. Note increasing LREE-enrichments at lower modal cpx (A–D) and similar patterns ($La/Sm_{PM} < 1$; $Sm/Yb_{PM} \gg 1$) for cpx in the majority of olivine-rich samples (E–H). Dashed lines in (C) show REE calculated for cpx in residues after different degrees of melt extraction after Ionov et al., 2002.

from olivine-rich rocks range broadly and in some samples are as high as those in cpx from fertile rocks (Figs. 3E and 4A). Normalised abundances of highly incompatible Th, U and Nb are not as high as for MREE and Sr (Figs. 3F and H). Nearly all Tok cpx have deep negative anomalies of Ti and Pb; negative Zr anomalies are less common.

Abundances of V, Yb, Nd and Nb in cpx (El_{cpx}) are plotted in Figs. 4A–D vs. $Cr\#_{spl}$ $[Cr/(Cr + Al)_{at}]$ as a par-

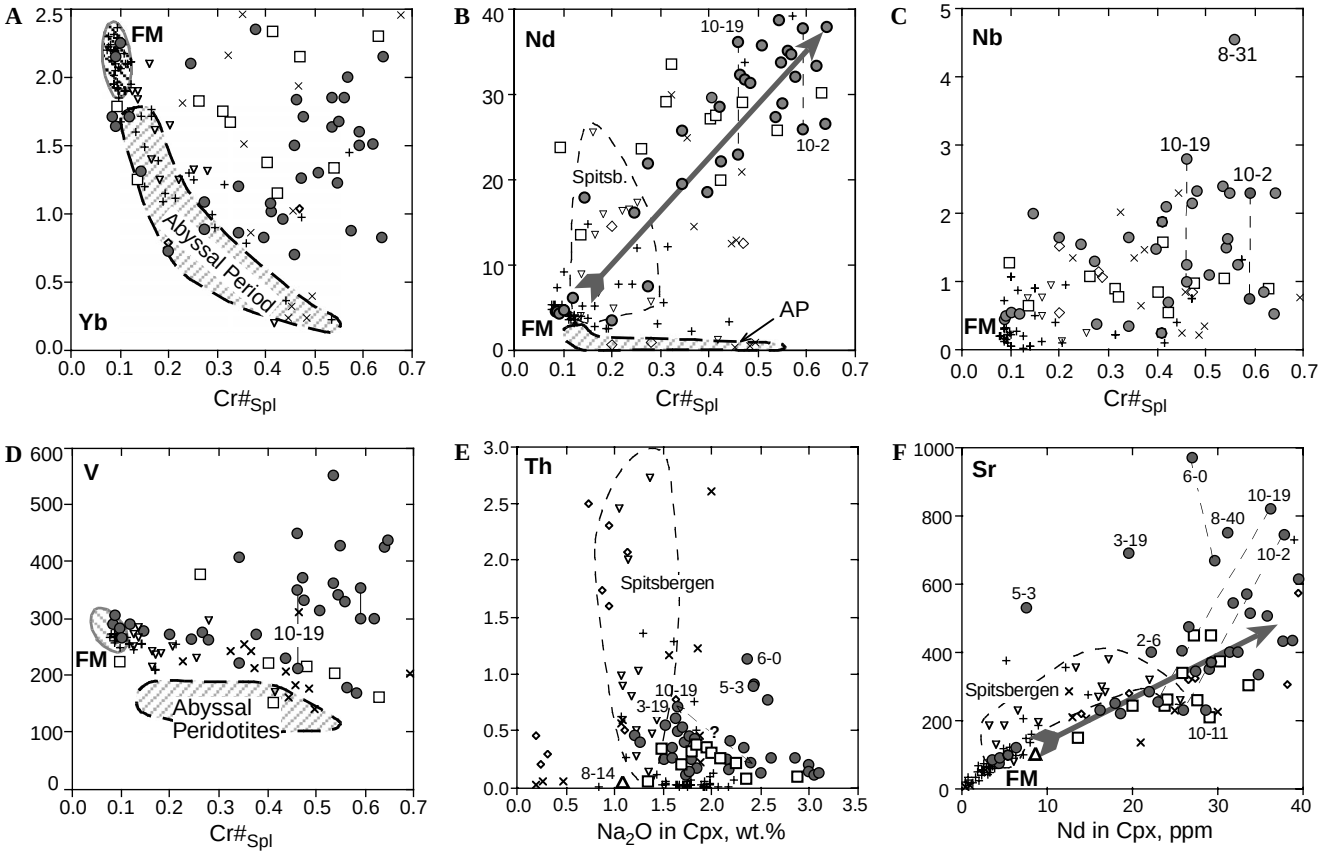

Fig. 4. Variation plots for trace element abundances in cpx (ppm) vs. $Cr\#_{Spl}$ $[Cr/(Cr + Al)_{at}]$ (A–D) and Na_2O in cpx (E) and for Sr vs. Nd (F). Filled circles, LH series peridotites; open squares, LW series peridotites; open triangle, cumulate 8–14. Also shown are abyssal peridotites (AP, hatched field) from the Atlantic and Indian oceans (Johnson et al., 1990; Ross and Elthon, 1997; Hellebrand et al., 2002) and spinel peridotite xenoliths from: crosses, Siberia and Mongolia (Stosch et al., 1986; Ionov et al., 1995a,b; Wiechert et al., 1997; Ionov et al., 2005b); diagonal crosses, Kerguelen (Mattielli et al., 1999; Grégoire et al., 2000); small upside-down triangles and dashed line field, Spitsbergen (Ionov et al., 2002); rhombs, Eifel (Witt-Eickschen et al., 2003). FM, fertile mantle. Straight dashed lines connect coexisting cpx generations in three samples. Grey arrows in (B) and (F) outline main metasomatic trend; cpx from phosphate-bearing LH series xenoliths are enriched in Sr relative to the trend in (F).

tial melting index. In general, cpx from refractory ($Cr\#_{spl} > 0.2$) Tok peridotites plot on those diagrams above the field of abyssal peridotites and do not comply with partial melting relationships (Hellebrand et al., 2001). Yb_{cpx} has a broad range (0.7–2.4 ppm) in the olivine-rich rocks but does not exceed values for fertile lherzolites (Fig. 4A). By contrast, Nd_{cpx} is positively correlated with $Cr\#_{spl}$ and is very high (25–40 ppm) at $Cr\#_{spl} \geqslant 0.5$ (Fig. 4B). The contents of highly incompatible Th, U, Nb show no regular correlations with $Cr\#_{spl}$ (Fig. 4C) or Na_{cpx} (Fig. 4F). The abundances of highly incompatible elements and V are commonly higher in cpx from the LH series rocks than in LW series cpx (Figs. 4B–F). Overall, the Tok cpx commonly have higher Nd and Sr (Figs. 4B and F) but lower or similar Th, Nb (Figs. 4C and E) than cpx in other metasomatised xenolith suites, like Spitsbergen.

For many olivine-rich Tok xenoliths, LA-ICPMS analyses of different cpx grains yield broad variation ranges, which greatly exceed analytical precision (see cpx 6–0, 10–2 and 10–19 in Table 4 and Fig. 4). These ranges may be as high as 10-fold for Ti and 2- to 5-fold for Zr, Nb, Sr, LREE, Pb and Th. To find out how these variations are related to cpx generations defined by optical microscopy and EPMA, two cpx types in sample 10–2 were analysed by SIMS (pit size <30 μm) at three inclusion-free spots near contacts to each other (cpx-A and cpx-B, Fig. 1B). The SIMS data yielded narrow abundance ranges (1σ/mean $\leqslant$ 15%) for REE, Y and V in cpx-A and cpx-B while HFSE (Ti, Nb, Zr and Hf), Sr and Th show significant scatter in one or both cpx types (up to 8-fold for Zr in cpx-A, Table 3). Regardless of the scatter, averaged SIMS values for REE, Sr, Nb and Th are significantly higher in the Na-rich cpx-A than in cpx-B, with smaller differences for MREE–HREE (Table 3 and Fig. 5). Averaged SIMS values for cpx-B are close to the average of two similar LA-ICPMS analyses of cpx 10–2 (LA-2, Fig. 5). Another LA-ICPMS analysis (LA-1, Table 4) yielded higher LREE, Th, U and Sr and lower HREE, Y, Zr and Hf than for LA-2, cpx-A and cpx-B. This analysis may correspond to a cpx type not sampled by the SIMS data. Overall, our results show that (a) coexisting Na-rich and Na-poor cpx may differ in abundances of REE, Sr and other trace elements and (b) broad variations of HFSE and Sr may also exist within each cpx type.

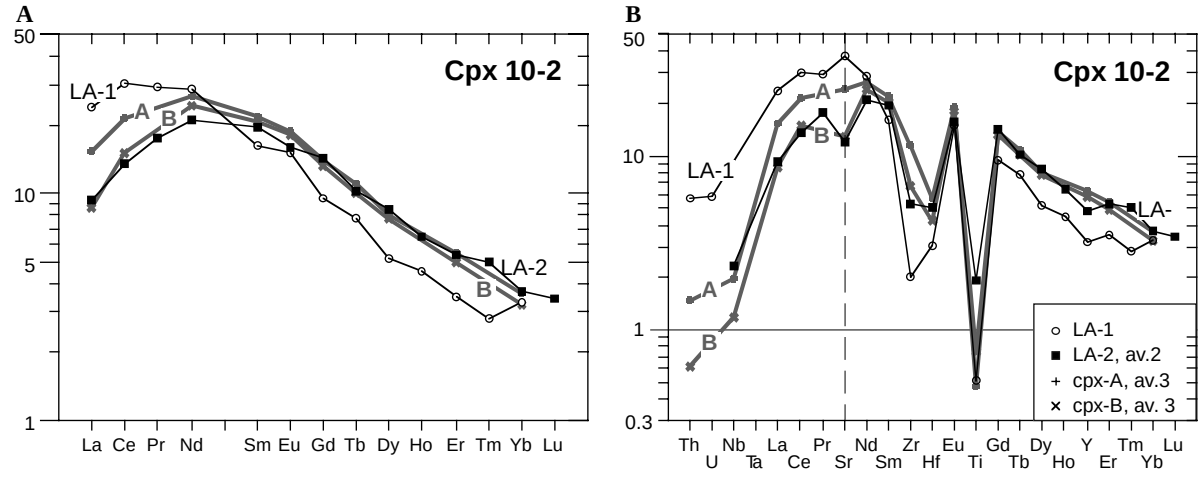

Fig. 5. Primitive mantle-normalised (Hofmann, 1988) REE (A) and multi-element (B) abundance patterns of cpx in xenolith 10–2 obtained by SIMS in thin sections (A and B; Fig. 1B, Table 3) and by LA-ICPMS in grain mounts (LA-1 and LA-2; Table 4). The B and LA-2 compositions are very similar indicating that LA-2 corresponds to the low-Na cpx; Na-rich cpx-A has higher abundances of incompatible trace elements (except Ti) than cpx-B.

4.2. Orthopyroxene and olivine

Representative trace element patterns of opx (Table 4) are shown in Fig. 6. REE_{PM} in opx from cpx-rich (>10%) LH series rocks decrease regularly from Lu to La. Opx 5–3 has spoon-shaped REE pattern with a bend at Gd (Fig. 6A), like for coexisting cpx (Fig. 3C). Opx from olivine-rich rocks (Fig. 6C) have mildly sinusoidal REE

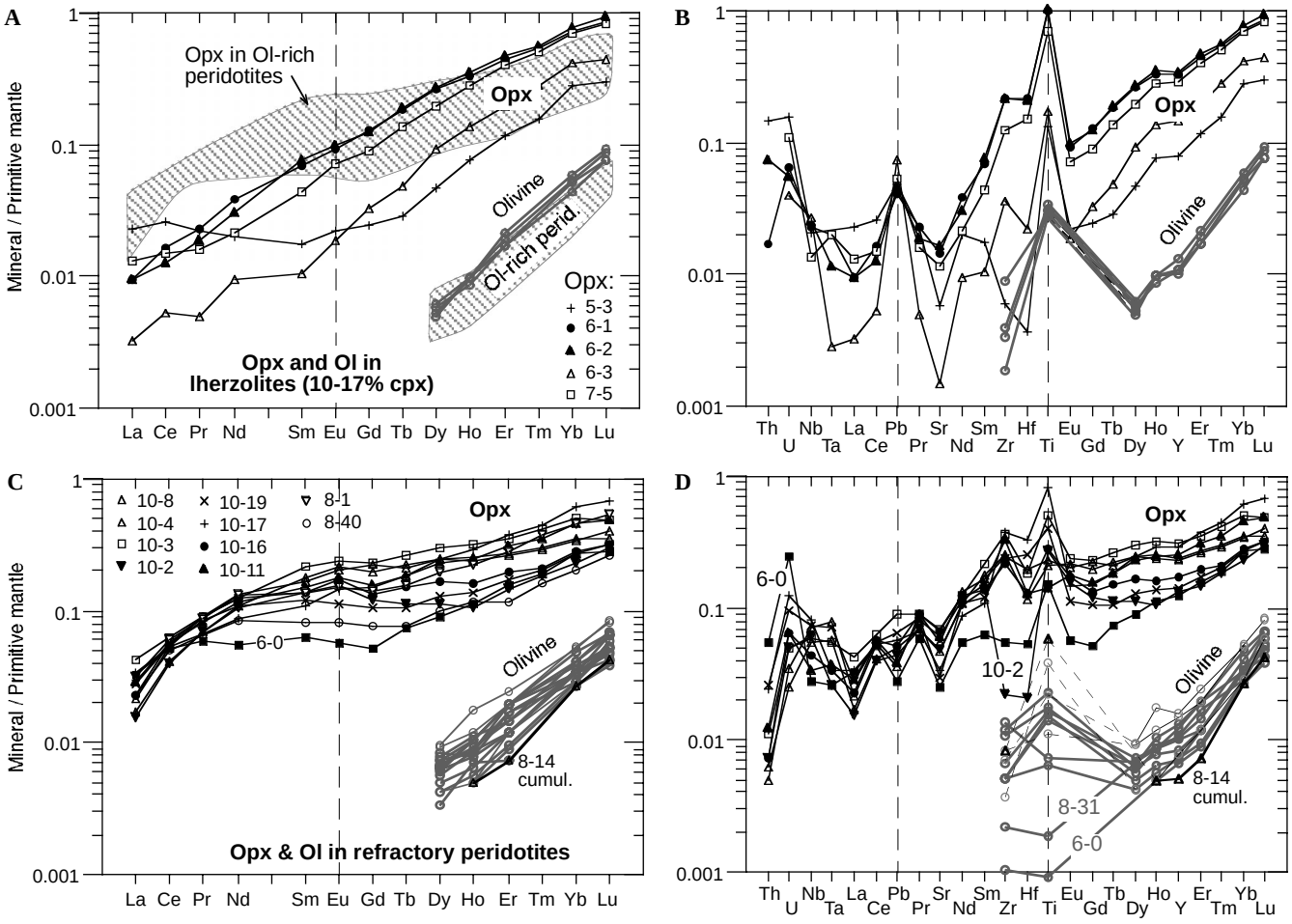

Fig. 6. Primitive mantle-normalised (Hofmann, 1988) REE (A and C) and multi-element (B and D) abundance patterns of opx and olivine (analysed at Mainz) in representative Tok xenoliths. Shaded areas in (A) outline the opx and ol fields for olivine-rich peridotites shown in (C).

patterns because of MREE–LREE "humps" superimposed on the general trend of decreasing REE_{PM} from Lu to La. Their LREE abundances are remarkably similar, in contrast to MREE–HREE. Positive anomalies of HFSE and U and negative Sr anomalies are common in Tok opx. Ti spikes in the opx decrease from fertile (Fig. 6B) to olivine-rich rocks (Fig. 6D); some opx have negative Zr–Hf anomalies.

The abundances of HREE and Y in olivine (Table 5) are 1–1.5 orders of magnitude lower than in coexisting opx (Figs. 6 and 7A) and define a tight array of patterns steeply declining from Lu to Dy. The abundance range of Ti and Zr is much broader than for the REE. The abundances of HREE, Zr, Ti in olivine and opx are positively correlated indicating chemical equilibrium (Fig. 7). An ol–cpx plot for Lu shows significant scatter (Fig. 7A), possibly related to chemically different cpx generations. We do not report data for less compatible elements because their analytical signals are "bumpy" and may be strongly affected by inclusions.

4.3. Accessory micro-phases

Phosphate minerals were initially found by optical microscopy and routine EPMA only in a small number of P-rich (0.11–0.16% P_2O_5) Tok xenoliths where they form

Table 5
Trace element composition of Tok olivines determined by LA-ICPMS (Mainz)

Sa. No.	Al	Ca	Sc	Ti	V	Mn	Co	Ni	Cu	Zn	Ge	Sr	Y	Zr	Nb	Dy	Ho	Er	Yb	Lu
LH series																				
6–0	46	267	2.3	1	1.2	955	128	2747	1.0	45	0.47		0.026	0.010	0.000		0.0007	0.0037	0.011	0.0025
7–5	143	509	3.0	30	3.3	1117	140	2746	1.4	47	0.56	0.001	0.040	0.018	0.002	0.0032	0.0014	0.0067	0.021	0.0049
8–1	110	461	3.3	17	3.7	1133	141	2842	1.0	49	0.57	0.006	0.028	0.049	0.005	0.0032	0.0009	0.0050	0.015	0.0034
8–2	94	414	3.1	7	3.3	1051	138	2882	1.9	55	0.56	0.026	0.029	0.049	0.012	0.0027	0.0008	0.0043	0.012	0.0033
8–3	77	356	3.0	18	3.4	1128	138	2932	0.8	64	0.53	0.013	0.049	0.064	0.003	0.0047	0.0012	0.0075	0.014	0.0041
8–5	158	516	3.0	30	3.6	1136	141	2810	1.5	58	0.58	0.010	0.043	0.086	0.005	0.0037	0.0012	0.0065	0.018	0.0049
8–6	159	510	2.9	37	3.4	1156	141	2702	1.6	51	0.60	0.004	0.051	0.038	0.002	0.0039	0.0014	0.0085	0.024	0.0060
8–7	76	361	3.4	8	3.5	1019	135	2799	1.3	50	0.58	0.007	0.040	0.132	0.005	0.0043	0.0012	0.0050	0.014	0.0031
8–8	84	367	3.1	19	3.2	1019	134	2874	1.0	52	0.50	0.014	0.043	0.105	0.007	0.0036	0.0012	0.0074	0.012	0.0037
8–11	78	364	2.8	15	3.6	1048	135	2893	0.9	52	0.42	0.005	0.051	0.049	0.005	0.0041	0.0015	0.0075	0.020	0.0043
8–31	50	288	2.1	2	1.0	1045	132	2872	1.0	55	0.50	0.004	0.041	0.021	0.001	0.0042	0.0013	0.0060	0.017	0.0042
8–39	132	495	2.8	33	3.4	1158	144	2725	1.6	49	0.55	0.005	0.043	0.032	0.002	0.0034	0.0014	0.0078	0.022	0.0055
8–50	120	527	3.5	25	3.9	1003	137	2864	1.4	49	0.53	0.009	0.033	0.116	0.008	0.0039	0.0011	0.0051	0.014	0.0027
10–2	49	338	1.8	6	1.9	1065	134	2793	0.9	52	0.45	0.005	0.045	0.030	0.002	0.0046	0.0015	0.0076	0.016	0.0034
10–4	67	358	2.8	5	1.4	1023	136	2875	0.9	54	0.59	0.005	0.044	0.058	0.002	0.0049	0.0016	0.0062	0.014	0.0033
10–8	79	370	2.6	9	3.2	1078	137	2802	1.2	58	0.60	0.009	0.044	0.048	0.004	0.0053	0.0011	0.0074	0.014	0.0030
10–16	66	372	2.4	19	2.3	1139	134	2642	1.5	57	0.51	0.006	0.030	0.044	0.003	0.0021	0.0010	0.0032	0.008	0.0027
10–17	117	461	2.6	26	3.1	1061	137	2710	1.9	48	0.50	0.005	0.040	0.066	0.004	0.0038	0.0015	0.0078	0.017	0.0044
10–19	62	355	3.1	10	3.4	1005	136	2864	1.6	48	0.50	0.012	0.025	0.029	0.005	0.0029	0.0006	0.0032	0.011	0.0026
LW series and cumulate																				
10–1	103	383	2.1	42	3.2	1477	130	2078	0.7	90	0.50	0.004	0.031	0.036	0.001	0.0027	0.0007	0.0046	0.012	0.0037
10–3	73	392	1.6	24	1.5	1805	130	2312	0.9	102	0.50	0.014	0.063	0.069	0.002	0.0061	0.0025	0.0103	0.021	0.0054
10–11	75	374	2.4	12	2.2	1782	136	2596	0.6	156	0.57	0.009	0.058	0.082	0.002	0.0058	0.0017	0.0076	0.022	0.0052
8–14	102	294	2.3	63	2.6	1662	177	994	0.6	92	0.63		0.020	0.08	0.002		0.0007	0.0030	0.011	0.0027

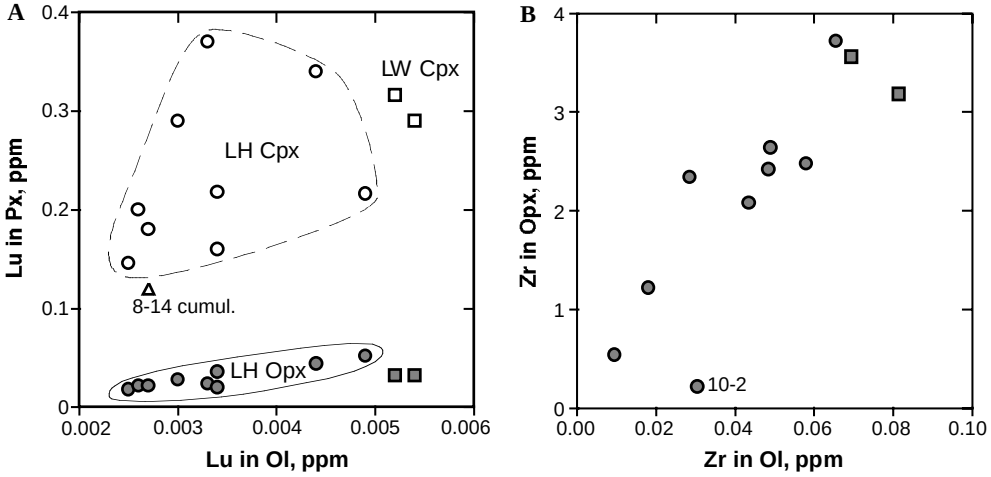

Fig. 7. Opx–cpx–olivine distribution plots for Lu (A) and Zr (B), in parts per million.

relatively large grains or aggregates (5–3, 8–40 and 10–19). Nevertheless, Ionov et al. (2005c,e) speculated that all Tok xenoliths with $\geqslant 0.03\%$ P_2O_5 contain phosphates assuming that major minerals of peridotites can host only trace amounts of phosphorus. In this study, we looked for accessory micro-phases in several Tok xenoliths (1–2 polished sections per sample) using EPMA element mapping in stage scanning mode with 1 μm steps registering signals for P, Ti, Nb, Zr and K and BSE images. Phosphates and Fe–Ti-oxides found by the mapping were analysed by EPMA using techniques optimised for specific trace elements.

Phosphates were detected in all xenoliths studied ($P_2O_5 \geqslant 0.06\%$) but their morphology and distribution are highly irregular. They usually occur as networks or clusters following certain grain boundaries and fine-grained pockets; interstitial materials away from those networks contain no phosphates. Only very small and rare apatite grains were detected in sections 10–11; because this sample has the highest P_2O_5 (0.23%) among the Tok xenoliths it may have very uneven phosphate distribution on hand-specimen scale. No grains suitable for EPMA (>2 μm across) were found in sample 10–2 (0.06% P_2O_5). However, interstitial pockets in that xenolith (Fig. 8A) contain numerous skeletal phosphate micro-phases (Fig. 8B) in a cryptocrystalline matrix, which is rich in alkali feldspar (Fig. 8D) and has high Ti contents (Fig. 8C).

Abundances of La, Ce, Nd, Sr and Cl in apatite and whitlockite from six xenoliths are given in Table 6. High-resolution data for whitlockite are only available for sample 8–40 because in other xenoliths whitlockite is intergrown with apatite on micrometer-scale. All the phosphates are rich in Sr (0.14–2.5% SrO) and LREE (900–3400 ppm La) and have high La/Nd_{PM} (2–4). Whitlockite has lower Sr and usually higher LREE than coexisting apatite.

EPMA mapping has shown that accessory phases with high Zr and Nb are very rare in the Tok peridotites, unlike for feldspar-bearing xenoliths from Sikhote-Alin (Kalfoun et al., 2002). Quantitative analyses were obtained for ilmenites from sample 10–4 (Table 7), which contain 4.6% Nb_2O_5 and 0.3–2.6% ZrO_2 and have tiny Zr-rich (~26% ZrO_2) inclusions.

4.4. Whole-rock compositions

Ionov et al. (2005c,e) presented whole-rock ICPMS data for a small number of Tok xenoliths. Here, we provide new solution ICMPS analyses for all 45 xenoliths in this study (including two full duplicates) and two host basalts (Table 8).

Fertile Tok peridotites have nearly flat REE patterns ($REE_{PM} \sim 1$; Fig. 9A). Refractory LH series rocks have low HREE abundances (0.1–0.4 × PM) and show consistent gradual enrichments from Ho to Nd (Fig. 9C). Their LREE patterns are commonly La-enriched ($La/Nd_{PM} > 1$), in particular for P-rich, phosphate-bearing samples (Fig. 9E). Harzburgites 8–50 and 10–17 have lower

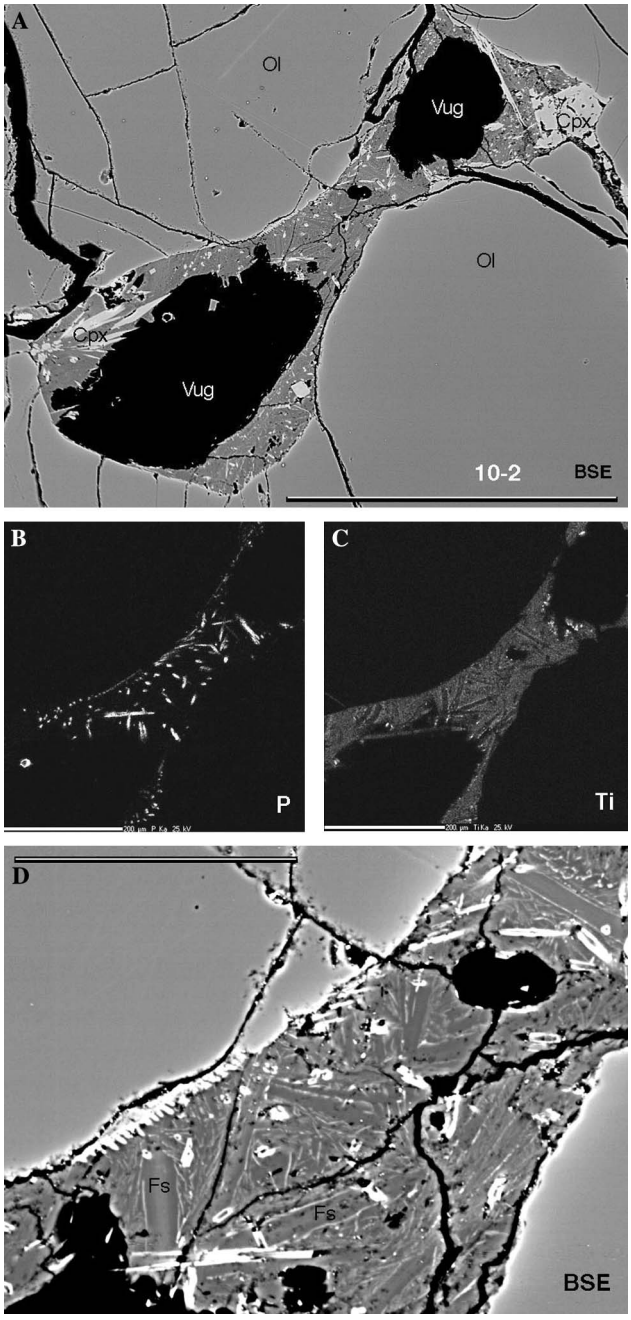

Fig. 8. (A) BSE image of a late-stage pocket with empty cavities in sample 10–2. Skeletal acicular crystals at bottom left and upper right are cpx (not apatite!). Symbols are same as in Fig. 1. Scale bar is 500 μm. Distribution maps of phosphorus (B) and Ti (C) in central part of the pocket shown in (A). The pocket contains needle-shaped phosphate grains; cryptocrystalline material between quench crystals is rich in Ti. Scale bars are 200 μm. (D) High-resolution BSE image of central part of the pocket shown in (A–C). Quench crystals of cpx, Fs and phosphates, which are too small to obtain good EPMA, can be identified using element distribution maps (e.g., B and C). Scale bar is 100 μm.

LREE–MREE than other LH series rocks. LW series rocks have much higher HREE (0.5–0.9 × PM) and MREE than refractory LH series rocks (Figs. 9C and G and 10A), consistent with higher modal cpx in the former (Table 1) and generally similar REE in the cpx (Fig. 3G). LREE abun-

Table 6
EPMA of apatite, whitlockite and their intergrowths

Sa. No.:	3–22	5–3				8–31			8–40		10–11	10–19			
Mineral:	Ap	Ap	Ap	Wh/Ap	Wh/Fs	Ap	Wh/Ap	Wh	Ap	Wh	Ap	Ap	Ap	Wh/Ap	Wh/Ap
Na_2O	0.42	0.38	0.28	2.30	2.35	0.11	2.80	2.84	0.09	2.49	0.00	0.25	0.38	2.06	1.50
MgO	0.59	0.50	0.44	3.16	3.30	0.24	3.22	3.19	0.15	3.52	1.82	0.56	0.62	3.29	3.31
P_2O_5	35.5	43.0	43.1	45.9	45.3	41.1	45.6	44.3	42.0	47.2	36.6	42.1	41.3	46.6	46.3
Cl	0.43	1.63	1.25	0.49	0.02	0.59	0.15	0.00	2.51	0.01	0.11	1.82	2.22	0.19	0.44
CaO	46.3	46.3	48.9	46.4	44.1	51.3	45.9	42.6	51.7	45.3	50.2	49.1	49.7	45.8	45.8
SrO	0.44	0.64	0.52	0.25	0.14	1.48	0.68	0.38	2.67	1.50	0.72	2.04	2.47	1.23	1.53
La_2O_3	0.11	0.17	0.19	0.22	0.19	0.18	0.29	0.31	0.10	0.26	0.14	0.17	0.12	0.21	0.39
Ce_2O_3	0.20	0.27	0.29	0.35	0.30	0.35	0.57	0.56	0.21	0.62	0.18	0.31	0.21	0.39	0.70
Nd_2O_3	0.09	0.11	0.11	0.11	0.10	0.15	0.25	0.25	0.08	0.26	0.08	0.14	0.09	0.17	0.27
Total[a]	84.1	93.1	95.1	99.2	95.7	95.5	99.5	94.5	99.6	101.1	89.9	96.5	97.1	99.9	100.2
Sr (ppm)	3740	5430	4380	2120	1160	12480	5770	3230	22,600	12700	6050	17,200	20,900	10,400	12,900
La (ppm)	970	1480	1600	1880	1590	1490	2510	2680	870	2250	1220	1470	980	1800	3360
Ce (ppm)	1730	2270	2490	2970	2530	3000	4820	4800	1830	5310	1550	2640	1750	3300	5970
Nd (ppm)	790	910	940	930	820	1320	2150	2110	680	2220	710	1170	760	1430	2330
La/Nd_{PM}	2.4	3.2	3.4	4.0	3.8	2.2	2.3 2.5	2.5	2.0	3.4	2.5	2.5	2.5	2.8	

Wh, whitlockite; Ap, apatite; Wh/Ap, Wh/Fs, whitlockite intergrown with minor apatite or feldspar.
Analyses reported in weight percentage for oxides and Cl; abundances of Sr and LREE are also given in ppm.
[a] Low totals are due to breakdown of phosphates under electron beam and/or effects of adjacent silicates for small phosphate grains.

Table 7
EPMA of Ti-rich oxides in sample 10–4

	Nb-ilmenite			Zr-Ilm 29
An. No.:	21	26	28	
SiO_2	1.89	1.08	0.76	1.54
TiO_2	45.66	46.92	47.44	29.99
Al_2O_3	0.64	0.26	0.20	0.55
Cr_2O_3	0.26	0.27	0.29	0.21
FeO	34.82	34.54	34.76	21.84
MgO	7.09	7.09	7.23	4.99
CaO	0.38	0.24	0.22	0.30
ZrO_2	0.32	2.58	1.55	26.04
Nb_2O_3	4.60	4.59	4.66	5.75
Total	95.67	97.57	97.10	91.20

Analysis 29 is for an inclusion in ilmenite.

dances in the LH and LW rocks partly overlap (Figs. 9C and 10B), e.g., P-rich LH xenoliths contain more La than the LW rocks (Figs. 9E and 10C). The La/Nd values in bulk peridotites are usually higher than in their cpx (cf. Figs. 3 and 9) indicating that much La in those rocks resides in inter-granular material rather than in the cpx.

Refractory LH series rocks typically have negative Ti and Pb anomalies (Fig. 9D) but they are not as deep as in cpx from the same samples (Figs. 3D–H). Some LREE-enriched xenoliths have marked negative anomalies of Zr, Hf and Nb (Figs. 9D and F) while other refractory Tok xenoliths have minor positive Zr and Nb anomalies (Figs. 9D and H).

Cumulate xenoliths have convex-upward trace element patterns, like many LW series rocks; the pattern of olivine-rich cumulate 8–44 is within the LW series field (Figs. 9G and H). Nonetheless, the cumulates can be distinguished from the olivine-rich LH and LW rocks by lower LREE/HREE and the absence of or much smaller negative Ti anomaly.

5. Discussion

5.1. Evidence for metasomatism from earlier work

Ionov et al. (2005c,e) concluded based on detailed petrographic and major oxide data on xenoliths from this study that non-cumulate Tok peridotites originally formed as residues after melt extraction at $\leqslant$3 GPa and that many of those residues later experienced enrichments in Fe, Ca, alkalis and precipitation of accessory phases. They used a small number of whole-rock ICPMS analyses to argue that: (1) LW series rocks are not cumulates and (2) late-stage interstitial materials were produced by mantle metasomatism rather than infiltration of host magma because trace elements ratios in the xenoliths are distinct from those of host basalts.

An important conclusion of the earlier work is that the metasomatism in the Tok mantle involved at least two stages. The first one was due to reactive percolation of evolved mafic melts, which turned some refractory residues (Mg# 0.90–0.92) into low Mg# (0.83–0.89), cpx-rich LW series rocks (Ionov et al., 2005c). Later on, volatile-rich phases, Na-rich cpx (out of equilibrium with normal mafic melts) and interstitial materials precipitated from alkali-rich media. Ionov et al. (2005c,e) did not explore trace element features of the metasomatism and the nature of the late-stage events, which are subjects of this study.

5.2. Role of partial melting and metasomatism in trace element compositions

Our data on highly incompatible elements in rocks and minerals show that enrichments in the Tok mantle were widespread and affected all rock types. Abundances of Th, U, La and Ce in fertile Tok xenoliths and their cpx

Table 8
Solution ICPMS analyses (in ppm) of whole-rock xenoliths and host basalt

Sa. No.:	BIR-1				JP-1			1–2	1–3	1–3a	1–13	2–1	2–2	2–3	2–4	2–6	2–9	2–10	3–2	3–4	3–19	3–22	5–3	6–0*	6–1	6–2	6–3	7–1	7–5
Series			av. 4	RSD (%)	Niig.	R.v.	21.11.2	LH	LH	LH	LH	LW	LW	LW	LW	LH	LH	LW	LW	LH	LH	LW	LH	LH	LH	LH	LH	LH	LH
Sc	44	43.8	40	9	7.5	7.24	7.24	9	6	7	6	9	9	8	11	9	6	15	7	2	8	9	11	6	16	16	12	8	16
Ti	5755	6036	5673	9	16.0		22	32	199	212	196	nd	nd	nd	nd	263	181	nd	nd	nd	381	607	80	60	1019	1051	311	258	720
V	313	322	300	4	18	28	37	61	51	51	42	81	90	87	86	65	45	114	86	62	69	54	69	23	87	89	67	51	100
Co	51	53	49	5	113	116	93	107	95	106	104	107	111	113	120	83	100	107	111	112	98.8	97	100	109	93	92	90	104	105
Ni	166	175	163		nd		nd	nd	2527	2830	2851	2016	2081	2181	2207	2108	2777	1905	2170	2280	nd	2335	2574	2259	2219	2201	2377	2797	nd
Cu	126	113	111		nd		nd	nd	2.1	2.5	1.8	7	24	6	10	0.8	3.7	24	4	1.	nd	2.3	7.7	2.3	14.9	13.8	5.3	2.3	nd
Zn	71	65	58	9	nd		61	51	39	42	41	81	74	67	76	46	35	59	77	50	52	70	39	nd	36	38	36	38	62.4
Ga	16	15.2	/13.4/		nd	0.7	nd	nd	0.7	0.7	0.9	2.7	2.8	2.7	2.9	1.1	0.6	4.4	2.3	1.8	nd	1.8	1.1	nd	2.2	2.3	1.9	0.8	nd
Rb	0.24	0.195	0.19	15	0.32	0.34	0.27	0.09	0.53	0.53	0.21	0.58	0.63	0.97	1.00	0.40	0.57	1.78	1.08	1.08	0.44	1.02	0.08	0.72	0.08	0.11	0.26	0.28	0.11
Sr	110	106	107	5	1.5	0.57	0.66	33.5	38.5	39.1	18.5	60.3	43.2	64.0	84.5	22.8	29.1	58.4	87	33.1	50.4	61.7	123	115	17.4	17.3	22.2	24.1	20.1
Y	16.5	16.2	16.2	4	0.11	0.10	0.10	0.89	2.25	2.25	1.19	6.40	3.53	4.21	5.53	1.45	1.01	5.31	4.38	1.94	2.10	3.87	1.56	1.71	4.02	4.25	1.58	1.90	3.5
Zr	14.5	14.5	15.7	4	5.5	5.34	5.57	1.80	7.73	7.71	8.40	31.9	12.6	12.1	22.0	10.4	3.41	24.1	27.2	17.3	10.0	38.0	0.76	3.96	8.36	8.67	6.54	10.4	4.9
Nb	0.55	0.56	0.59	6	0.044	0.036	0.044	0.63	1.46	1.49	0.99	1.32	1.40	2.03	1.79	0.75	1.45	2.30	3.32	2.51	1.14	4.20	0.44	2.09	0.22	0.27	0.85	1.33	0.32
Cs	0.005	0.005	0.005	18	0.039	0.035	0.042	0.001	0.005	0.005	0.005	0.006	0.005	0.007	0.008	0.006	0.004	0.013	0.012	0.013	0.006	0.018	0.002	0.009	0.002	0.002	0.002	0.004	0.002
Ba	6.4	6.52	6.63	4	10.0	9.8	9.7	4.0	4.5	4.3	2.2	8.6	9.8	14.6	15.5	5.1	7.5	26.3	20.0	10.2	10.0	22.6	6.7	17.7	2.4	1.7	4.4	3.9	7.0
La	0.58	0.60	0.66	6	0.028	0.030	0.030	1.64	1.64	1.60	1.03	1.94	1.33	2.09	2.87	1.40	1.28	1.43	2.42	1.55	2.30	1.88	7.51	10.5	0.45	0.45	0.89	1.07	0.85
Ce	1.85	1.90	2.04	5	0.062	0.054	0.076	4.09	3.89	3.93	2.28	5.59	3.62	5.82	7.28	3.25	2.90	4.65	6.63	3.31	5.00	5.74	11.5	18.4	1.16	1.06	2.17	2.61	1.72
Pr	0.37	0.38	0.39	6	0.008	0.007	0.006	0.53	0.57	0.58	0.31	0.95	0.56	0.89	1.11	0.42	0.37	0.82	1.05	0.43	0.65	0.96	1.07	1.79	0.16	0.16	0.29	0.38	0.21
Nd	2.35	2.38	2.43	3	0.031	0.033	0.040	2.26	2.66	2.63	1.35	5.02	2.84	4.32	5.24	1.92	1.57	4.33	5.24	1.85	2.66	4.83	3.23	6.45	0.86	0.90	1.33	1.89	0.91
Sm	1.10	1.12	1.12	3	0.009	0.013	0.010	0.45	0.65	0.62	0.30	1.46	0.76	1.07	1.29	0.40	0.31	1.12	1.35	0.44	0.60	1.28	0.39	0.92	0.32	0.34	0.29	0.48	0.26
Eu	0.52	0.52	0.52	3	0.003	0.003	0.003	0.14	0.22	0.20	0.10	0.49	0.26	0.34	0.42	0.13	0.10	0.37	0.44	0.14	0.18	0.41	0.13	0.28	0.12	0.13	0.10	0.16	0.10
Gd	0.38	0.38	0.37	1	0.003	0.0026	0.0021	0.30	0.58	0.57	0.28	1.51	0.78	1.04	1.21	0.39	0.25	1.09	1.23	0.41	0.48	1.18	0.27	0.64	0.48	0.50	0.27	0.48	0.36
Tb	1.97	1.85	1.82	2	0.011	0.013	0.013	0.04	0.08	0.08	0.04	0.23	0.11	0.15	0.18	0.05	0.04	0.16	0.17	0.06	0.07	0.16	0.04	0.08	0.09	0.09	0.04	0.07	0.07
Dy	2.5	2.53	2.51	2	0.014	0.018	0.017	0.19	0.43	0.41	0.22	1.20	0.63	0.78	0.92	0.27	0.17	0.92	0.87	0.32	0.39	0.83	0.22	0.40	0.59	0.62	0.24	0.37	0.48
Ho	0.57	0.59	0.57	1	0.004	0.004	0.004	0.03	0.08	0.08	0.04	0.23	0.12	0.14	0.17	0.05	0.03	0.18	0.15	0.06	0.07	0.14	0.05	0.06	0.13	0.14	0.05	0.07	0.11
Er	1.7	1.73	1.70	4	0.013	0.014	0.013	0.07	0.20	0.19	0.11	0.58	0.29	0.35	0.46	0.13	0.08	0.46	0.37	0.17	0.18	0.33	0.13	0.16	0.41	0.42	0.16	0.17	0.32
Yb	1.6	1.65	1.61	3	0.019	0.021	0.021	0.05	0.15	0.15	0.09	0.41	0.24	0.26	0.35	0.11	0.08	0.38	0.25	0.15	0.16	0.24	0.15	0.11	0.40	0.42	0.16	0.13	0.33
Lu	0.25	0.25	0.25	3	0.004	0.0047	0.0041	0.007	0.020	0.022	0.014	0.058	0.035	0.040	0.051	0.018	0.014	0.055	0.036	0.023	0.025	0.032	0.024	0.018	0.064	0.062	0.026	0.019	0.054
Hf	0.56	0.56	0.59	3	0.118	0.120	0.120	0.03	0.12	0.12	0.15	0.69	0.27	0.25	0.44	0.20	0.05	0.50	0.45	0.32	0.20	0.81	0.01	0.06	0.22	0.23	0.14	0.18	0.14
Ta	0.06	0.04	0.04	5	0.005	0.004	0.004	0.017	0.062	0.062	0.059	0.075	0.079	0.091	0.092	0.064	0.041	0.132	0.159	0.138	0.056	0.194	0.004	nd	0.010	0.014	0.050	0.077	0.007
Pb	3	2.97	3.06	4	0.10	0.09	0.07	0.14	0.23	0.23	0.20	0.46	0.68	0.21	0.35	0.15	0.12	0.64	0.31	0.61	0.19	0.13	0.33	024	0.27	0.23	0.22	0.11	0.24
Th	0.03	0.03	0.03	14	0.013	0.012	0.013	0.049	0.062	0.075	0.062	0.088	0.095	0.106	0.180	0.077	0.071	0.074	0.146	0.161	0.168	0.066	0.388	0.87	0.036	0.040	0.056	0.050	0.083
U	0.01	0.01	0.01	13	0.012	0.012	0.012	0.028	0.028	0.031	0.027	0.041	0.049	0.046	0.059	0.022	0.037	0.036	0.068	0.058	0.056	0.030	0.112	0.22	0.016	0.017	0.022	0.020	0.031

Sa. No.:	8–1	8–2	8–3	8–5	8–5a	8–6	8–7	8–8	8–10	8–11	8–31	8–39	8–40	8–50	10–1	10–2	10–3	10–4	10–8	10–11	10–16	10–17	10–19	8–14	8–44*	8–1b	Stk-51*
Series	LH	LH	LH	LH	LH	LH	LH	LH	LW	LH	LH	LH	LH	LH	LW	LH	LW	LH	LH	LW	LH	LH	LH	Cumul.	Cumul.	Basalt	Basalt
Sc	11	9	5	12	12	14	7	5	9	8	7	10	9	8	13	6	8	7	8	6	14	8	9	47	12	nd	17
Ti	366	98	nd	570	572	804	nd	nd	nd	195	133	nd	134	299	1900	245	500	nd	172	306	nd	345	167	6590	1680	14160	14090
V	64	61	73	69	68	86	71	71	100	53	34	117	54	54	102	49	51	43	48	52	66	47	54	256	106	182	188
Co	102	97	114	97	100	90	116	112	118	104	100	109	101	105	91	102	99	120	108	109	128	108	105	58	133	43	45
Ni	2655	2562	2405	2454	2529	nd	2475	2381	1996	2774	2772	1847	2718	2815	1808	2623	2260	2675	2870	2415	2355	2744	2818	nd	1280	nd	232
Cu	1.4	3.1	2.9	8.0	8.2	nd	7.5	1.1	6.9	2.2	1.4	25	6.5	4.8	17	3.1	1.5	2.5	2.2	2.2	11	5.0	3.7	nd	26	nd	44
Zn	40	40	81	45	44	44	42	53	68	42	41	38	36	40	69	41	76	58	42	123	63	48	39	37	nd	80	nd
Ga	1.9	0.9	1.7	2.0	1.9	nd	0.9	1.3	3.5	0.8	1.0	2.7	0.7	0.9	3.5	0.9	1.5	1.0	0.9	1.5	1.3	1.4	0.8	nd	nd	nd	nd
Rb	0.86	0.15	0.93	0.26	0.24	0.16	0.69	0.62	0.59	0.30	0.31	0.14	0.74	0.29	1.07	0.34	0.42	0.53	0.15	0.75	bd	0.35	0.19	1.71	0.65	30.1	31.3
Sr	27.1	28.1	31.2	28.0	28.0	27.9	34.1	25.4	85.1	39.4	70.8	27.6	92.3	14.4	86.7	45.7	71.4	32.3	26.3	85.1	37.5	9.9	78.6	120	51	1089	1036
Y	136	1.13	1.82	2.21	2.18	3.73	1.54	1.39	5.10	1.65	2.49	4.66	1.54	0.79	4.97	2.12	4.62	1.18	1.41	3.49	1.40	1.10	1.32	12.1	4.68	24.9	20.6
Zr	7.26	7.51	11.8	17.0	17.1	9.5	21.0	12.8	18.1	7.91	12.5	9.86	2.48	7.35	16.8	11.2	37.1	9.75	9.01	14.9	11.3	5.63	4.25	46.4	18.0	269	224
Nb	1.07	0.27	1.27	0.75	0.75	0.55	1.33	1.44	1.55	0.41	4.60	0.55	0.93	0.79	1.87	4.47	1.47	3.44	2.50	0.57	1.50	0.57	0.52	2.36	2.56	76	113
Cs	0.019	0.001	0.011	0.002	0.003	0.001	0.007	0.007	0.006	0.002	0.002	0.002	0.010	0.005	0.008	0.003	0.002	0.005	0.002	0.014	0.001	0.008	0.003	0.018	0.010	0.53	0.48

(*continued on next page*)

Table 8 (*continued*)

Sa. No.:	8–1	8–2	8–3	8–5	8–5a	8–6	8–7	8–8	8–10	8–11	8–31	8–39	8–40	8–50	10–1	10–2	10–3	10–4	10–8	10–11	10–16	10–17	10–19	8–14	8–44*	8–1b	Stk-51*
Series	LH	LH	LH	LH	LH	LH	LH	LH	LW	LH	LH	LH	LH	LH	LW	LH	LW	LH	LH	LW	LH	LH	LH	Cumul.	Cumul.	Basalt	Basalt
Ba	43.4	1.4	11.0	4.6	4.6	2.2	4.9	8.5	15.4	6.4	6.1	2.9	10.3	2.3	29.8	10.6	7.1	2.7	3.1	10.7	3.6	5.0	9.3	37.7	11.5	475	452
La	1.33	1.54	1.56	0.86	0.87	1.11	1.52	1.05	2.22	0.81	3.56	0.91	6.73	0.64	2.06	2.13	1.79	1.18	0.72	8.57	0.85	0.39	5.85	3.58	1.73	47.8	46.7
Ce	3.30	3.79	3.38	2.61	2.60	2.64	3.45	2.55	5.35	2.11	7.45	1.87	14.5	1.52	5.44	5.12	5.52	2.57	2.48	16.4	2.94	1.03	10.7	10.5	4.36	91.2	89.3
Pr	0.46	0.50	0.45	0.43	0.44	0.36	0.50	0.36	0.83	0.32	0.95	0.23	1.72	0.21	0.83	0.71	0.92	0.33	0.43	1.90	0.46	0.14	1.17	1.75	0.63	10.4	10.4
Nd	2.06	2.08	1.97	2.07	2.06	1.64	2.24	1.68	4.11	1.64	3.91	1.07	6.03	093	3.96	3.16	4.53	1.44	1.93	7.21	2.05	0.61	4.06	9.40	3.31	41.1	41.4
Sm	0.38	0.38	0.45	0.46	0.45	0.43	0.51	0.38	1.11	0.42	0.83	0.32	0.83	0.19	1.12	0.69	1.26	0.32	0.41	1.32	0.44	0.14	0.56	2.73	0.94	8.00	7.59
Eu	0.11	0.11	0.14	0.14	0.13	0.16	0.15	0.12	0.36	0.14	0.24	0.13	0.23	0.06	0.38	0.23	0.42	0.10	0.13	0.39	0.13	0.05	0.16	0.97	0.35	2.55	2.50
Gd	0.32	0.29	0.41	0.40	0.40	0.53	0.40	0.33	1.10	0.38	0.69	0.49	0.54	0.18	1.21	0.60	1.20	0.29	0.36	1.09	0.33	0.17	0.42	2.94	1.17	6.99	6.65
Tb	0.04	0.04	0.06	0.06	0.06	0.09	0.05	0.05	0.16	0.06	0.09	0.09	0.07	0.03	0.17	0.08	0.18	0.04	0.05	0.14	0.04	0.03	0.05	0.46	0.18	0.95	0.86
Dy	0.23	0.19	0.30	0.33	0.35	0.59	0.27	0.23	0.90	0.31	0.46	0.63	0.27	0.13	0.96	0.39	0.93	0.20	0.25	0.68	0.23	0.16	0.23	2.52	1.10	4.88	4.73
Ho	0.05	0.04	0.06	0.07	0.08	0.13	0.05	0.04	0.17	0.06	0.08	0.15	0.05	0.03	0.18	0.07	0.17	0.04	0.05	0.12	0.04	0.04	0.04	0.45	0.21	0.87	0.81
Er	0.12	0.10	0.16	0.20	0.21	0.37	0.12	0.12	0.43	0.15	0.20	0.42	0.11	0.07	0.47	0.19	0.41	0.10	0.13	0.30	0.11	0.12	0.12	1.14	0.52	2.22	2.02
Yb	0.13	0.10	0.13	0.20	0.21	0.35	0.10	0.10	0.32	0.12	0.17	0.41	0.08	0.07	0.35	0.14	0.30	0.08	0.10	0.23	0.095	0.12	0.09	0.80	0.41	1.54	1.50
Lu	0.019	0.016	0.018	0.032	0.037	0.059	0.016	0.016	0.043	0.019	0.022	0.067	0.013	0.011	0.052	0.020	0.043	0.012	0.014	0.033	0.016	0.020	0.015	0.11	0.062	0.22	0.22
Hf	0.14	0.09	0.20	0.27	0.26	0.24	0.24	0.21	0.40	0.12	0.20	0.22	0.05	0.11	0.49	0.13	0.71	0.11	0.15	0.26	0.18	0.11	0.08	1.60	0.47	5.29	3.86
Ta	0.060	0.031	0.068	0.056	0.057	0.033	0.086	0.092	0.083	0.032	0.145	0.021	0.040	0.041	0.105	0.139	0.085	0.122	0.111	0.035	0.064	0.037	0.016	0.19	nd	4.28	nd
Pb	0.12	0.12	0.20	0.13	0.15	0.15	0.21	0.16	0.31	0.17	0.20	0.24	0.74	0.27	0.33	0.11	0.12	0.13	0.05	0.19	0.24	0.15	0.24	1.05	0.24	4.18	3.12
Th	0.095	0.080	0.128	0.050	0.060	0.076	0.094	0.077	0.174	0.041	0.154	0.119	0.156	0.051	0.144	0.081	0.042	0.063	0.022	0.36	0.024	0.023	0.32	0.19	0.15	5.28	5.30
U	0.031	0.032	0.044	0.024	0.032	0.026	0.044	0.028	0.047	0.030	0.069	0.058	0.087	0.024	0.082	0.037	0.020	0.030	0.012	0.131	0.027	0.014	0.12	0.081	0.059	1.69	1.66

nd, not determined; bd, below detection. Three samples marked with asterisk were analysed at CRPG (Nancy, France), the remainder were analysed at the Grenoble laboratory. 1–3a and 8–5a are full duplicates of samples 1–3 and 8–5.

are higher than estimated for residues of low degrees of partial melting (Figs. 3A–C and 9A and B). All olivine-rich peridotites in this study are strongly enriched in light and middle REE over HREE; the Tok suite differs in this regard from many other olivine-rich xenolith suites worldwide (South Africa, NW USA, Patagonia, Kerguelen and Canary Islands), which usually include LREE-depleted and/or poorly metasomatised refractory rocks (Mattielli et al., 1999; Grégoire et al., 2000; Neumann et al., 2002; Peslier et al., 2002; Rivalenti et al., 2004; Grégoire et al., 2005). Another distinctive feature of olivine-rich Tok peridotites is consistently high abundances of MREE (20–40 ppm Nd) and Sr (250–1000 ppm) in their cpx (Figs. 3E and G), which greatly exceed those reported for refractory off-craton xenoliths in nearby southern Siberia and Mongolia (Fig. 4). Although similar or even higher MREE and Sr contents in cpx were found in other mantle peridotites, e.g., from Kerguelen and Canary Islands (Mattielli et al., 1999; Grégoire et al., 2000; Neumann et al., 2002), such samples are rare in those xenolith suites.

HREE are generally less affected by mantle metasomatism than lithophile elements with lower compatibilities in mantle peridotites and are considered robust partial melting indices (McDonough and Frey, 1989; Bodinier and Godard, 2003; Pearson et al., 2003; and references therein). Yet, HREE abundances in nearly all refractory ($Al_2O_3 < 2\%$ and $Cr\#_{Spl} > 0.2$) LH series rocks and their cpx are decoupled from modal and chemical indicators of partial melting (e.g., Figs. 4A and 10A) and are usually higher than for poorly metasomatised abyssal or massif peridotites (Johnson et al., 1990; Takazawa et al., 2000; Hellebrand et al., 2001) indicating strong metasomatic enrichments. The latter are also apparent from elevated FeO and Ca/Al in many LH series rocks (Fig. 7 in Ionov et al., 2005e). LW series rocks have highest HREE among Tok peridotites (Fig. 10A) due to abundant metasomatic cpx.

Altogether, the geochemical data on the Tok xenoliths indicate large-scale metasomatic re-working of their original residual 'protoliths'. This transformation typically erases chemical evidence for the melting events in refractory peridotites (at least for incompatible lithophile trace elements) and imparts geochemical signatures of enriched fluids. These results, together with mineralogical and major element data, characterise the uppermost mantle beneath the Tok area as one of the most strongly metasomatised continental mantle domains worldwide.

5.3. Trace element residence in metasomatised peridotites

5.3.1. REE and Sr

Fig. 10 shows that six olivine-rich peridotites are distinguished from the remainder of Tok xenoliths by much higher La (3.6–10.5 ppm vs. $\leqslant$2.4 ppm) and have the highest P_2O_5 (0.07–0.23% vs. $\leqslant$0.06%; Fig. 10D). By contrast, the abundances of Nd (Fig. 10B) and MREE in the same samples are much closer to averages for the Tok suite,

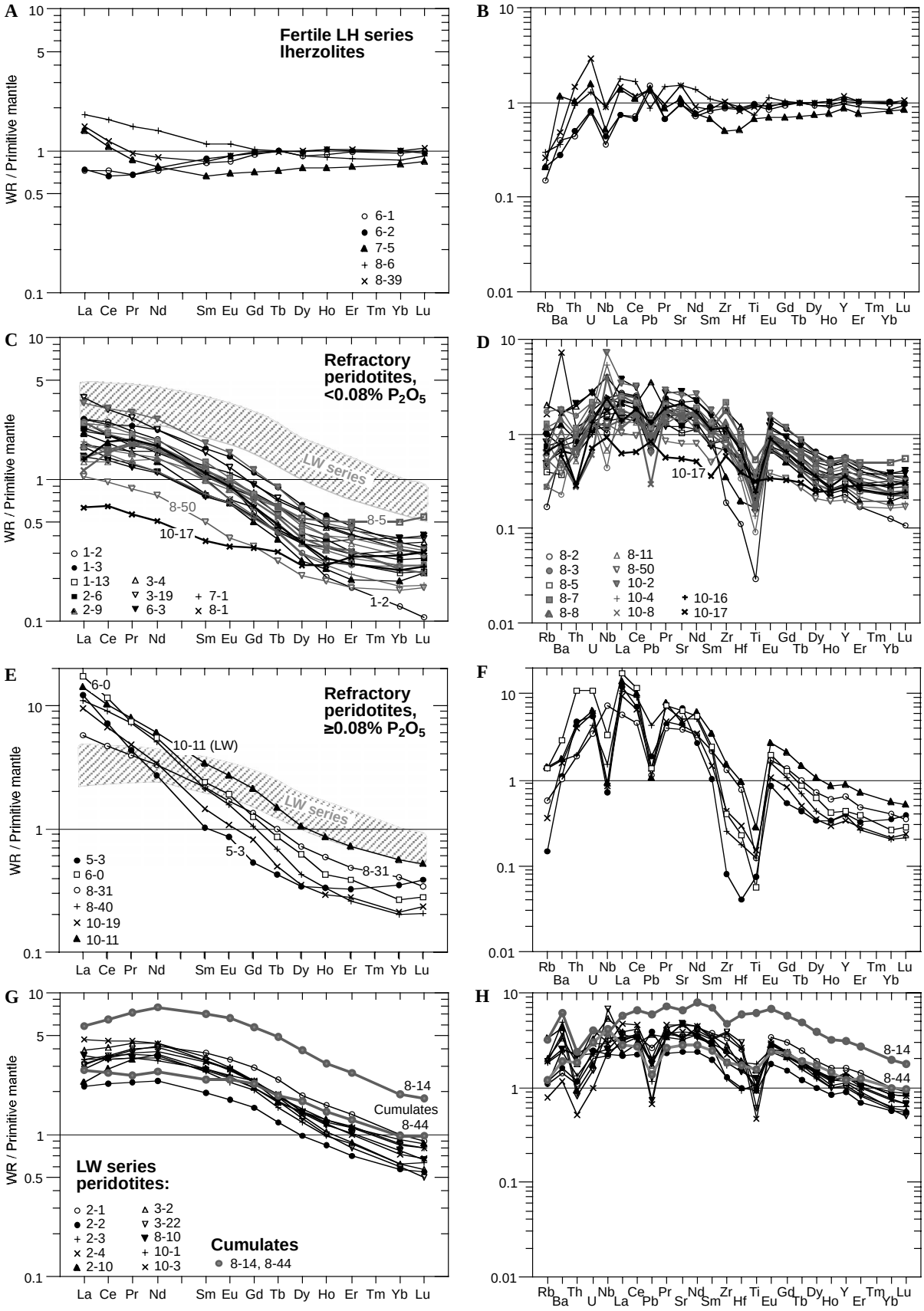

Fig. 9. (A–H) Primitive mantle-normalised (Hofmann, 1988) REE (left) and multi-element abundance patterns of whole-rock Tok peridotites. HREE and MREE in LW series rocks are much higher than in refractory LH rocks (mainly because of higher modal cpx). Phosphorus-rich xenoliths (Ionov et al., 2005c,e) have high LREE, high La/Nd_{PM} (E) and negative anomalies of HFSE and Pb (F). Cumulate xenoliths differ from LW series rocks by lower ratios of highly to moderately incompatible elements and higher Ti/Eu.

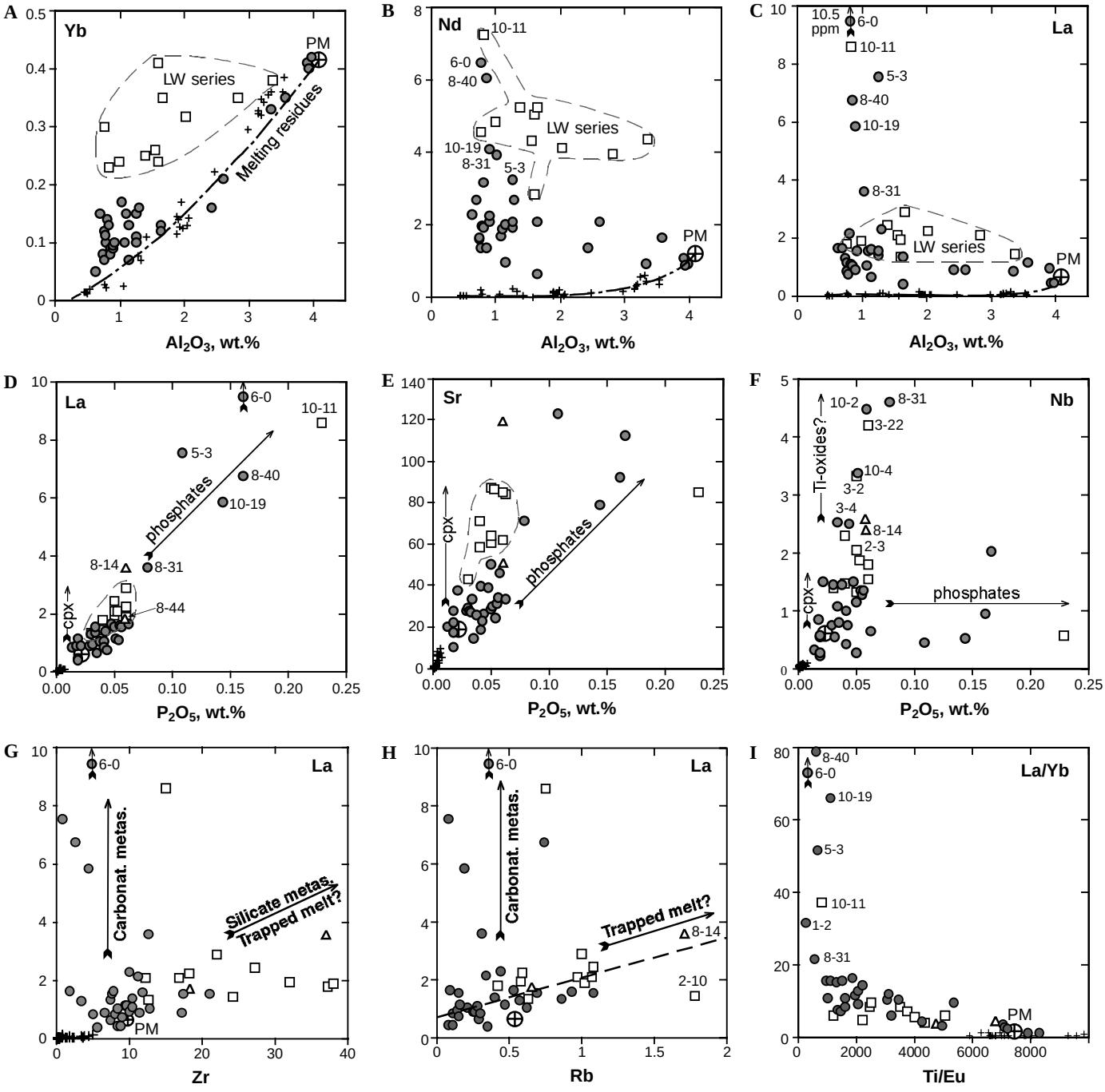

Fig. 10. Variation plots for whole-rock abundances of trace elements (ppm) vs. Al_2O_3 (A–C), P_2O_5 (D–F) and inter-element diagrams (G–I). Filled circles, LH series Tok peridotites; open squares, LW series Tok peridotites; triangles, ol–cpx cumulates. Also shown in (A–C) are unmetasomatised Horoman peridotites (crosses) and melt extraction trends at 1 GPa (dashed lines) after Takazawa et al. (2000). PM, primitive mantle (Hofmann, 1988). P_2O_5 values are after Ionov et al. (2005c,e). Arrows indicate contributions of different minerals in whole-rock element budgets (D–F) and inferred trends of chemical change for different types of metasomatism (H and I). Dashed line in (H) is linear La–Rb correlation ($r^2 = 0.53$) excluding samples with Rb >1.2 ppm and $P_2O_5 \geqslant 0.06\%$.

and their La/Nd_{PM} range from 1.8 to 4.7. In all the La-rich xenoliths, petrographic inspection and mineral mapping found phosphate grains, which are big enough for EPMA (Table 6). The phosphates yield both very high La (900–3400 ppm, i.e., about two orders of magnitude higher than in coexisting cpx; Fig. 11) and consistently high La/Nd_{PM} (2–4). As shown in Fig. 11, cpx in the La-rich xenoliths has either $La/Nd_{PM} > 1$, like in the whole-rocks and coexisting apatite (sample 5–3), or $La/Nd_{PM} < 1$ (10–11). The phosphates are unevenly distributed in sample 10–11 (Section 4.3) and appear to be out of equilibrium with the cpx outside the phosphate-rich domains; these domains may be of late-stage origin. Mass balance estimates show that the share of whole-rock La hosted by cpx is low (6% in 10–

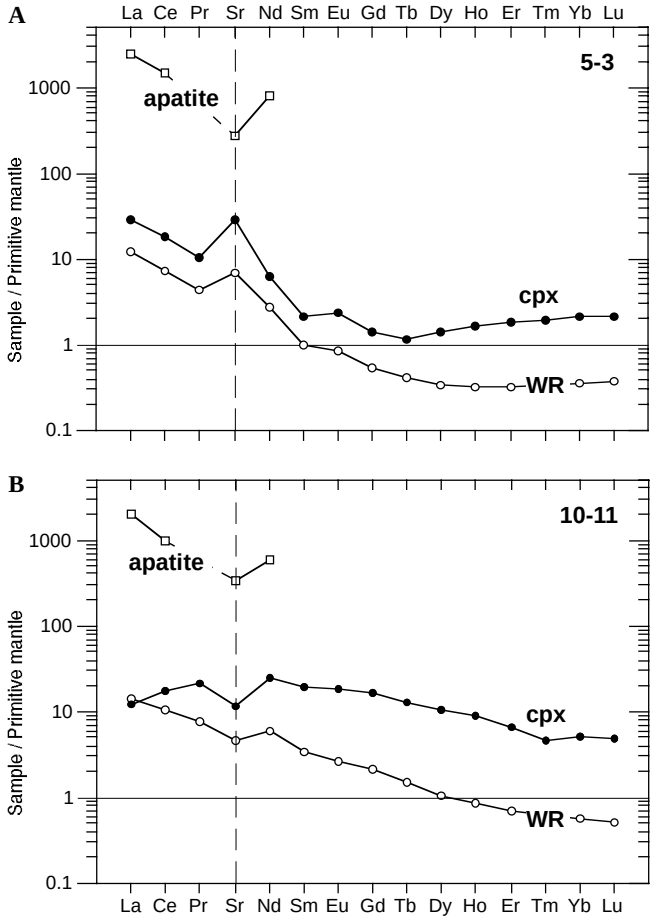

Fig. 11. Primitive mantle-normalised (Hofmann, 1988) REE-Sr abundance patterns of whole-rocks (WR), cpx and apatite in LH series xenolith 5–3 (A) and LW series xenolith 10–11 (B). WR and cpx have consistent Sr anomalies in both samples. By contrast, cpx 10–11 has $La/Nd_{PM} < 1$ while its WR has $La/Nd_{PM} > 1$; their LREE patterns converge at La. The LREE–MREE patterns in cpx and WR 5–3 are nearly parallel.

11 and 20% in 5–3), with most of the remainder residing in phosphates (>60% in 10–11 and >50% in 5–3). The latter values are approximate because the LREE range in phosphates may not have been well constrained with the small number of EPMA done for each sample. Altogether, the mineralogical and trace element evidence firmly establishes a link between strong enrichments of the bulk peridotites in La and the presence of phosphates in the Tok xenoliths. Such links can also be demonstrated for Ce, Th and U.

Phosphates are important hosts also of other LREE and Sr, but the share of those elements residing in the cpx is higher than for La (20–40% for Nd and Sr in 5–3 and 10–11), consistent with higher cpx/melt partition coefficients ($^{cpx/melt}D_{El}$). Assuming that sample 5–3 only contains apatite (which has higher Sr than coexisting whitlockite), the estimated share of apatite in the whole-rock budget of Sr is ~10%, i.e., much lower than for cpx (40%). Correspondingly, plots of Sr (Fig. 10E) or Nd vs. P_2O_5 show positive trends (fairly vague) only for P_2O_5-rich xenoliths while whole-rock Sr and Nd in other samples are more affected by variations in modal cpx. In particular, LW series rocks tend to have higher Sr than LH series rocks with $P_2O_5 \leqslant 0.06\%$ (Fig. 10E) in line with higher modal cpx. Furthermore, the apatite typically has negative Sr anomalies (i.e., low Sr/Nd) whereas coexisting cpx and the bulk rocks may have positive Sr anomalies (Fig. 11). The role of apatite in whole-rock budgets of LREE, Sr, Th and U was earlier addressed by other mantle xenolith suites (e.g., Ionov et al., 1997; Bedini and Bodinier, 1999; Pearson et al., 2003). The data on whitlockite obtained in this study are not sufficient to constrain its specific role in the distribution of Sr and LREE in the Tok suite.

Phosphate-bearing fine-grained to cryptocrystalline materials (Fig. 8) appear to have formed by quenching of interstitial melts rich in phosphorus and alkalis shortly before or during the transport of the xenoliths to the surface. Their solidification may have been assisted by a loss of abundant volatile components (see vugs in Fig. 8). Because no phosphates were found by EPMA mapping outside the quenched materials in sample 10–2 it appears that a large proportion of P and LREE in that sample was hosted by the interstitial melt at the time when the xenolith was trapped by the host magma, i.e., mantle metasomatism was still in progress. The presence of cpx generations and broad ranges of LREE, Sr and other elements in cpx 10–2 (Figs. 1B, 4F and 5F) may be related to the late-stage metasomatism.

Opx and olivine host only negligible proportions of LREE and Sr in the bulk rocks but they are significant hosts of the HREE. Mass balance estimates (Tables 1, 4 and 5) show that cpx and opx host 50–70% and 20–30% Lu, respectively, in Tok peridotites; the share of Lu in olivine ranges from 5% to 7% for fertile lherzolites to 10–20% in olivine-rich rocks.

5.3.2. HFSE and alkalis

Earlier xenolith studies have shown that accessory phl, amph, Ti-rich oxides and feldspar may be important hosts of HFSE and alkalis (e.g., Ionov and Hofmann, 1995; Bodinier et al., 1996; Ionov et al., 1999; Grégoire et al., 2000; Laurora et al., 2001; Pearson et al., 2003). Indeed, relatively high Nb and Ta in several Tok xenoliths (3–2, 3–4 and 2–3; Fig. 10F) appear to be related to the presence of phl (Fig. 1F) and amph, which concentrate Nb (57–188 ppm) and Ta (2–9 ppm, Table 4). However, no "hydrous" minerals have been found in four xenoliths with highest Nb abundances (Fig. 10F), which instead contain cryptocrystalline materials with high Ti contents (Fig. 8); the latter may be important hosts of HFSE. EPMA mapping in Tok xenoliths found few Ti-oxide grains rich in Zr and Nb; thus the latter are unlikely to be as important hosts for Nb and Zr in the Tok suite as for xenoliths from other sites in the Russian Far East (Ionov et al., 1999; Kalfoun et al., 2002). There are no apparent links between high Nb or Zr and high P_2O_5 or La (Figs. 10F and G) consistent with low HFSE in apatite (e.g., Ionov et al., 1997). Abundances of Zr, but not Nb, in the cpx-rich LW series rocks are higher than in LH series rocks consistent with higher compatibility of Zr than Nb in the cpx.

Opx, in addition to cpx, is an important host of Ti in all LH series Tok peridotites, even though Ti spikes in opx are absent or much smaller in refractory than in fertile rocks (Fig. 6). The major reason for the latter is that many olivine-rich rocks are depleted in Ti (Fig. 9). Furthermore, positive Ti anomalies in the opx are complementary to negative Ti anomalies in coexisting cpx (Figs. 3B and D) and result from stronger partitioning of Ti from cpx to opx compared to MREE. The magnitudes of the Ti anomalies (Ti/Eu variations; Fig. 10I) are controlled by closed-system cpx–opx distribution of Ti and MREE dependant on temperature (Witt-Eickschen and O'Neill, 2005) and modal cpx/opx such that higher modal cpx in the fertile rocks can host a greater share of MREE and thus cause higher Ti spikes in coexisting opx.

The majority of Tok xenoliths with high Rb abundances (0.7–1.8 ppm; Fig. 10H) have phl, which is a major host of Rb (60–125 ppm; Table 4), or its breakdown products. Rb contents in amph are two orders of magnitude lower, consistent with data on mantle xenoliths worldwide (Ionov et al., 1997). Furthermore, some phl-poor, feldspar-rich Tok xenoliths, like 3–22, have much Rb (~1 ppm) as well. Alkali-rich feldspar may be an important host of Rb (and Ba) in such rocks, e.g., high Rb (25–100 ppm) and Ba were earlier reported for metasomatic feldspar from other xenolith suites in southern Siberia (Ionov et al., 1999; Kalfoun et al., 2002).

5.4. Trace element composition of metasomatic media

The convex-upward trace element patterns typical of cpx from olivine-rich Tok peridotites (Figs. 3E–H) are normally considered as evidence for equilibration with LREE-enriched silicate liquids (e.g., McDonough and Frey, 1989; Ionov et al., 1994; Bedini et al., 1997; Ionov et al., 2002; Bodinier and Godard, 2003). PM-normalised abundances of trace elements in the cpx are related to $^{cpx/melt}D_{El}$, i.e., they increase from moderately incompatible Yb to Nd and decrease again for less compatible elements. The range of REE_{PM} from Gd to Pr in the majority of the cpx is quite narrow (Figs. 3E and G) regardless of modal and major oxide differences between the xenoliths and thus may have been buffered by metasomatic liquids with similar REE levels. Here, we constrain trace element abundances in such liquids using compositions of several Tok cpx with convex-upward patterns and relevant $^{cpx/melt}D$ from experimental work.

Fig. 12 shows element patterns for hypothetical liquids in equilibrium with two cpx from refractory LH series peridotites and cumulate cpx 8–14 calculated using $^{cpx/melt}D$ compiled by Ionov et al. (2002) mainly after Hart and Dunn (1993). Abundances of REE, Y, Ti, Zr and Hf calculated for a parental liquid of the cumulate cpx are very close to those in basalts hosting the xenoliths while the estimates for Sr, Nb, Th and U in the liquid are a little lower than in the basalt. Thus, the parental liquids for the Tok cumulates may not be very different from the intra-plate alkali basaltic magmas that brought up the xenoliths to the surface as suggested earlier based on Mg# and other major element data (Ionov et al., 2005c). This inference is supported by the fact that many of the cumulates have cryptocrystalline to fine-grained interstitial material with vesicles (Ionov et al., 2005c) and thus formed shortly before the entrapment into the host magma, possibly at an earlier stage of the same magmatic event.

Parental liquids calculated for cpx 10–2 (LA-2 in Fig. 5) and 10–4 have fractionated, LREE-enriched patterns as well. However, the calculated abundances of REE, Th, U, Nb, Pb, Zr and Hf in those liquids are about 2–3 times higher than in the host basalt while Ti contents are several times lower than in the basalt (Fig. 12). Qualitatively similar patterns are obtained for parental liquids of all Tok cpx with concave-upward patterns, except that some have deep negative Zr and Hf anomalies. All those liquids have

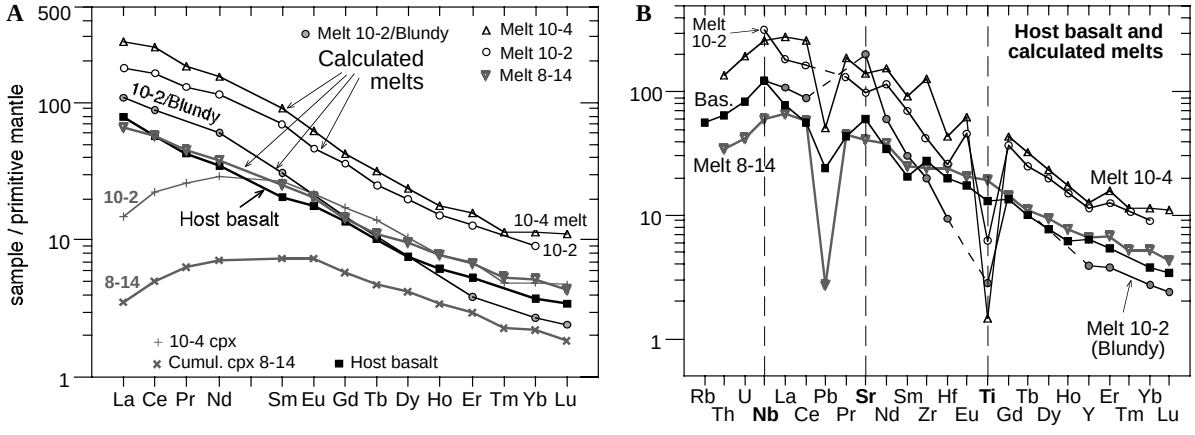

Fig. 12. Primitive mantle-normalised (Hofmann, 1988) REE (A) and multi-element (B) abundance patterns of hypothetical silicate melts in equilibrium with cpx from three Tok xenoliths calculated using partition coefficients ($^{cpx/melt}D$) from a compilation of Ionov et al. (2002) and after Blundy et al., 1998. The pattern calculated for cumulate 8–14 is nearly identical to that of host basalt; those for cpx from two refractory xenoliths are distinct from the host basalt regardless of the choice of $^{cpx/melt}D$.

higher REE, Y, Sr, Th and U than that for cumulate cpx 8–14; olivine 8–14 also has lower abundances of HREE and Y than olivine from refractory Tok peridotites (Fig. 6). We see those estimates as an indication that hypothetical melts or fluids responsible for the dominant convex-upward trace element patterns of the Tok cpx are distinct from the host alkali basaltic magma, in particular, they have strong negative Ti anomalies and higher abundances of incompatible trace elements. The variable but usually low abundances of Ti, Zr and Hf inferred for those media (Figs. 3E–H and 12) may indicate an origin in a different tectonic setting (e.g., subduction-related).

It is important to assess if such a conclusion is dependant on the choice of $^{cpx/melt}D$, which may vary with temperature (T), pressure (P) and phase compositions (e.g., McDade et al., 2003). Blundy et al. (1998) found that $^{cpx/melt}D$ during incipient melting of fertile peridotites may be significantly higher than those established by Hart and Dunn (1993). High $^{cpx/melt}D$ had been earlier obtained for cpx micro-phenocrysts in alkali-rich glasses in mantle xenoliths (Ionov et al., 1994; Chazot et al., 1996). In particular, Ionov et al., 1994 showed that $^{cpx/melt}D_{HREE}$ increase from 0.3 to 0.4 (like in Hart and Dunn, 1993) to 1.6 with higher contents of alkalis, Al_2O_3 and SiO_2 and lower MgO and CaO in the melt.

REE abundances in liquids in equilibrium with cpx 10–2 and 10–4 calculated using $^{cpx/melt}D$ values after Blundy et al. (1998) are much closer to REE in the host basalt than those using $^{cpx/melt}D$ after Hart and Dunn (1993). Nevertheless, the calculated melts differ from the host basalt by higher Sr and LREE/HREE, steeper pattern slopes from Gd to Nd (which have narrow abundance ranges in the Tok cpx; Figs. 3E and G) and, in particular, deep negative Ti anomalies. It is not clear which $^{cpx/melt}D$ set is more appropriate for the metasomatised Tok peridotites; moreover, the major element composition and T regime of the metasomatic media may have varied considerably and cannot be constrained with sufficient certainty. $^{cpx/melt}D$ of Hart and Dunn (1993) may better suit refractory peridotites (like olivine-rich Tok xenoliths) at high P–T (e.g., McDade et al., 2003); they also yield reasonable results for cumulates from Tok (Fig. 12) and ophiolites (Koga et al., 2001). On the other hand, the set of Blundy et al. (1998) may be appropriate at low-T and high Na in the melt (Gaetani, 2004) consistent with high Na_2O in Tok cpx (Ionov et al., 2005c,e). In any case, all the model estimates indicate that: (1) cpx in the majority of olivine-rich Tok xenoliths equilibrated with evolved, LREE-enriched silicate liquids; (2) the liquids have strong negative Ti anomalies, which persist regardless of the choice of $^{cpx/melt}D$ for mafic melts (Fig. 12B).

Several Tok xenoliths have strong LREE-enrichments in cpx (Fig. 3C) and bulk rocks (Figs. 9E and 10) as well as negative HFSE anomalies, high Zr/Hf (Fig. 9F) and low Ti/Eu at high La/Yb (Fig. 10I). Quite a few xenolith studies attributed such signatures to equilibration with (or entrapment of) exotic, carbonatite, or carbonate-rich melts (Hauri et al., 1993; Ionov et al., 1993; Rudnick et al., 1993; Yaxley et al., 1998; Mattielli et al., 1999). However, theoretical modelling and data on other peridotite series indicate that fractionated patterns with extreme LREE-enrichments may also be produced by coupled "chromatographic" effects and reactions at decreasing melt mass during percolation of moderately enriched basaltic melts (Bodinier et al., 1990; Harte et al., 1993; Bedini et al., 1997; Ionov et al., 2002; Rivalenti et al., 2004). Hence, the LREE-enriched patterns alone do not provide unequivocal evidence for the existence of a peculiar, carbonate-rich melt, distinct from liquids responsible for concave-upward patterns in the majority of the Tok cpx. Rather, those patterns can be attributed to fractionation of closely related metasomatic melts in "percolation columns" (Fig. 13) controlled by distances from their sources, porosity, host mineralogy etc. Extreme LREE-enrichments appear in transient derivatives of such melts at low melt/rock ratios close to the percolation front; they may be associated with strong chemical evolution of the melt from an originally basaltic composition to low-T, small-volume carbonate-rich melts, but do not necessitate a separate (e.g., carbonatite) melt source (Ionov et al., 2002; Bodinier et al., 2004; Rivalenti et al., 2004).

Chromatographic effects of melt percolation may also be a major reason why cpx from olivine-rich Tok peridotites has a broader range of HREE than for Nd to Gd (e.g., 4-fold for Yb and only 2-fold for Nd; Figs. 3E and G, 4A and B). LREE-enriched metasomatic media have high LREE but low HREE compared to melting residues (cell #1 in Fig. 13). Moreover, $^{cpx/melt}D_{LREE}$ (<0.2) are lower than $^{cpx/melt}D_{HREE}$ (>0.4) (Hart and Dunn, 1993; Gaetani, 2004) while opx and olivine are important hosts for the HREE but not for the LREE (Fig. 6). Hence, greater amounts of metasomatic melts may be needed to equilibrate HREE than LREE in residual peridotites. In other words, such melts can buffer the LREE–MREE in the host peridotites at lower melt/rock ratios than the HREE; these differences are enhanced by chromatographic fractionation during melt percolation (Navon and Stolper, 1987; Bodinier et al., 1990) and may cause complete peridotite–melt equilibration for LREE–MREE and incomplete equilibration for HREE at certain distances from melt sources (cell #x in Fig. 13).

To sum up, complete or advanced equilibration of olivine-rich peridotites with media enriched in highly incompatible elements ("cryptic" metasomatism) can be identified as a major enrichment event in the Tok mantle. The range of LREE–MREE from dominant concave-upward to LREE-enriched patterns as well as broad HREE variations in Tok cpx could be seen as evidence for origins from two or more types of such media and/or significant compositional variations in each type. We argue, however, that at least some, and possibly a large part, of those variations could rather be attributed to fractionation of a single initial melt (or a series of closely related melts) during its percolation in host peridotites. This major metasomatic

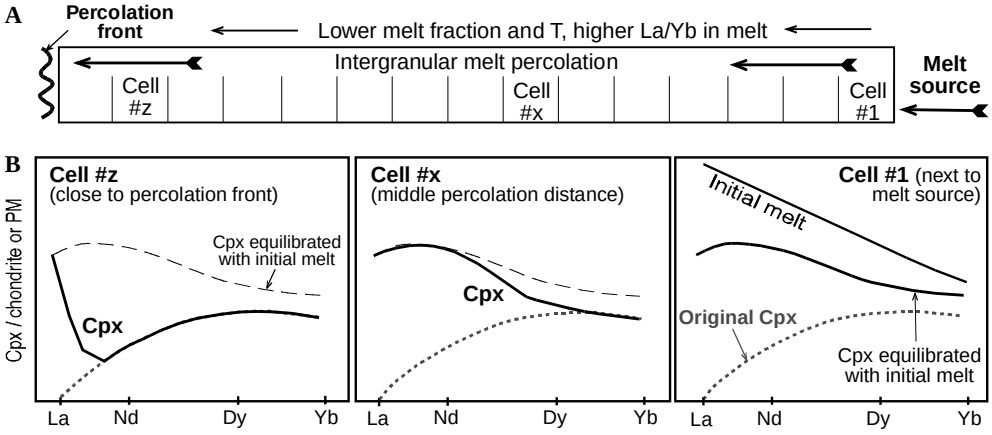

Fig. 13. A cartoon and REE pattern diagrams illustrating basic features of trace element fractionation during porous flow of LREE-enriched liquids in LREE-depleted peridotites based on numerical modelling; modified after Ionov et al. (2002): (A) melt percolates away from its source (e.g., a vein or the base of the lithosphere) in the inter-granular space of host peridotite. Percolation front is the most remote point reached by the melt coming from this source at each given moment, in other words the percolation front separates initial depleted peridotites from rocks where incipient melt percolation begins. For the sake of modelling, the "percolation column" between the melt source and the percolation front is divided into a certain number of "cells"; the melt is considered to advance stepwise from one cell to the next one. Within a given cell #x, each model increment may include the following sequence of processes: melt infiltration from cell #$x-1$; melt–rock reaction; mineral–melt re-equilibration (Vernières et al., 1997). (B) The modelling shows that the trace element composition of the melt (and hence of host peridotite) may change dramatically along the percolation column. One reason for that is that heavier REE partition from the melt into the host rock much more effectively than the lighter REE because they have higher peridotite/melt partition coefficients. As a result, the melt batches near the percolation front are more depleted in HREE and MREE than in LREE and thus have high La/Nd and La/Yb. It follows that as the percolation goes on, host peridotite near the melt source (cell #1) soon reaches trace element equilibrium with the initial melt, whereas far from the source (cell #z) both percolating melt and host peridotite are selectively enriched in highly incompatible elements relative to more compatible elements. In addition to the so-called "chromatographic" effects illustrated here, the melts are also likely to experience fractional crystallisation as they approach the percolation front at lower T, which decreases the melt fraction and increases the abundances of incompatible trace elements. The latter processes may also result in dramatic changes in the chemical composition of the initial liquid: from high-T basaltic melts to low-T, small-volume melts or fluids rich in alkalis, phosphorus and volatiles (Bodinier et al., 2004).

event was followed by localised, small-scale enrichments produced by a series of small-volume, late-stage alkali-rich fluids with variable but generally high P_2O_5 and CO_2.

5.5. The nature and sequence of metasomatic episodes in the Tok mantle

Studies of mantle rocks have defined several "types" of metasomatism attributed to a variety of media and processes: cryptic (anhydrous), modal (by hydrous melts), carbonatite, alkaline, feldspar–Ti-oxide, Fe-rich (±Ti) etc. Most of those types can be identified in the Tok xenolith suite indicating a complex enrichment history. Below we outline the nature and sequence of metasomatic events and their role in trace element enrichments in the Tok mantle.

5.5.1. Stage 1. Widespread metasomatism by pervasive melt percolation

The earliest metasomatic event in the Tok mantle, which can be constrained by chemical evidence, is probably the formation of the LW series (opx-poor lherzolites and wehrlites with low Mg#) accompanied by smaller (Fe, Ca)-enrichments in some LH series rocks. Ionov et al. (2005c) concluded based on petrographic and major element data in combination with numerical modelling of Fe–Mg solid/liquid exchange during melt percolation that the LW series was formed by reaction of host refractory peridotites with evolved silica under-saturated mafic melts. Such a process requires basaltic melts that have both high Fe contents (similar to those in peridotites) and moderately low Mg# (0.6–0.7 compared to Mg 0.76 in equilibrium with fertile mantle) as well as high time-integrated melt/rock ratios. Thus, the LW series rocks must have formed at high-T near the dry peridotite solidus, which for moderately refractory (3.5% Al_2O_3) Tinaquillo peridotite is ~1315 °C at 1.5 GPa (McDade et al., 2003).

The LW series rocks are equilibrated at much lower T (910–1020 °C; Table 1) and must have cooled to ambient temperatures after their formation. Xenolith equilibration T's likely follow a local P–T gradient in the lithospheric mantle at the time of entrainment in host magma; the dominant LH series rocks have a similar T range (870–1010 °C). Thus, the LW and the LH series rocks coexist in the depth range sampled by the Tok xenoliths (Ionov et al., 2005c) except that the LW rocks may be absent in its uppermost part corresponding to $T = 870$–910 °C (Figs. 14A and 15). The generally even distribution of the two series in the mantle profile may indicate that the LW series rocks trace fossil melt flow channels (zones with abundant veins or high-porosity peridotites) in the LH series wall-rocks (Fig. 15).

One could speculate that metasomatism in the LH series rocks was caused by residual fluids escaping from such melt channels to produce zoned metasomatic aureoles in host peridotites, with a range of enrichment styles controlled by distances from the channels (e.g., Bodinier et al.,

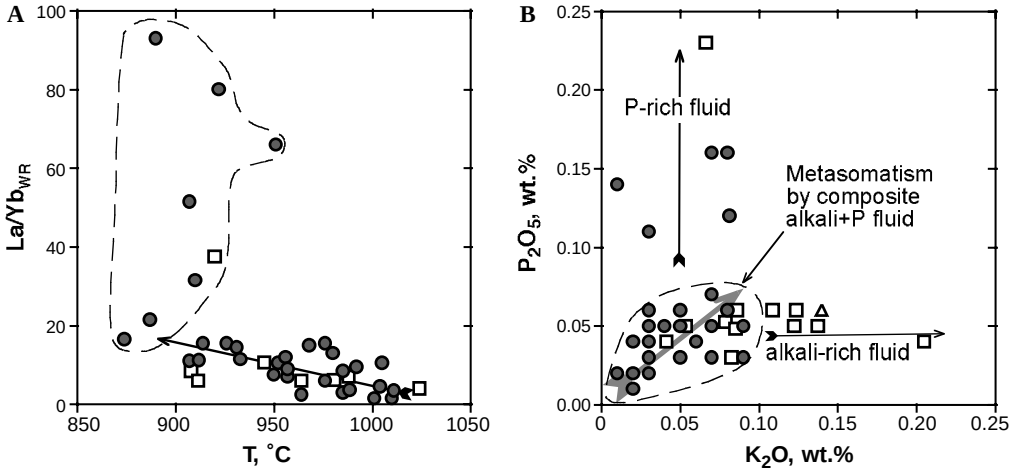

Fig. 14. (A) Plot of xenolith equilibration temperatures (T, Table 1) vs. La/Yb in bulk rocks. La/Yb is negatively correlated with T (and hence with the depth of origin) at La/Yb $\leqslant$20. All xenoliths with strong LREE-enrichments (La/Yb $\geqslant$20) have $T \leqslant$ 920–950 °C and hence come from shallow depths. (B) Plot of K_2O vs. P_2O_5 (data from Ionov et al., 2005c,e). A rough positive correlation exists at K_2O and $P_2O_5 < 0.1\%$ indicating metasomatism by a single (P, K)-rich fluid. By contrast, P-rich samples (containing coarse phosphates) show no matching K-enrichments and were probably precipitated from a separate P-rich fluid. Similarly, strong K-enrichments are not matched by equally high P and may indicate a distinct K-rich fluid or phl precipitation.

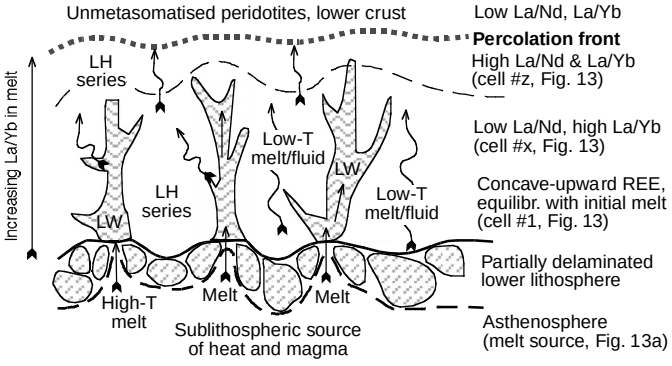

Fig. 15. A cartoon illustrating the scheme of the main metasomatic event in the Tok mantle by large-scale upward percolation and fractionation of basaltic melts. We speculate that an upwelling of hot asthenospheric mantle delaminated the base of the lithosphere and was the source of heat and magma for the metasomatism. First batches of high-T melt provided by that source moved upwards in high-porosity zones and reacted with refractory host peridotites to produce the LW series rocks. Simultaneously or shortly afterwards, frontal upward percolation of low-T melts took place in the CLM and caused metasomatism as long as the source of those melts remained active. The uppermost level in the CLM reached by those melts is shown as "percolation front". The metasomatic enrichment patterns can be roughly correlated with depth (Fig. 14A) and thus with relative position in the percolation column as shown in Fig. 13 (see notes to the right of the cartoon).

2004). The latter, however, does not appear to be the case for refractory LH series rocks because all of them are strongly metasomatised and show similar enrichment patterns (Figs. 3A–H and 4B), which would require a widespread, dense and regular network of fluid sources. Most importantly, whole-rock La/Yb is negatively correlated with T (Fig. 14A) (i.e., depth) such that the LREE-enrichments gradually increase upwards in the lithospheric section and are particularly strong and variable in the shallow mantle. Those correlations rather indicate ubiquitous large-scale upward migration of melts and fluids in the lithosphere, with high-T mafic melts channelled into high-permeability zones and low-T melts and fluids simultaneously propagating upwards by frontal percolation (Fig. 15). Because olivine-rich rocks are most permeable for basaltic liquids (Toramaru and Fujii, 1986) the metasomatic melts percolate much better in refractory than in fertile peridotites; the latter are usually poorly metasomatised (Figs. 3A and B). Chromatographic fractionation during percolation together with fractional crystallisation of the melt and decreasing porosity due to lower T caused strong enrichments in highly incompatible elements (Fig. 3C) close to the percolation front in the shallow mantle as discussed in previous section. Trace element equilibration with less fractionated melts at deeper levels (i.e., far from the percolation front) produced the dominant MREE-enriched, convex-upward trace element patterns in the cpx (Fig. 3) and smaller but ubiquitous Gd–La humps in coexisting opx (Fig. 6C) from refractory LH series rocks.

If the above scheme is correct, trace element signatures in cpx from the LW series and refractory LH rocks may be different due to equilibration with different derivatives of the initial melt (mafic high-T for the former vs. more evolved, low-T for the latter). Indeed, the abundances of highly incompatible elements (e.g., Sr, Nd, Nb and Th; Fig. 4) tend to be higher in the LH cpx, consistent with equilibration with more evolved liquids. On the other hand, those differences are small, and the element patterns of the cpx in the two rock series define nearly identical fields (Figs. 3E–H). Moreover, Na_2O contents in cpx from the LW series rocks (1.3–2.9%) are too high for cpx equilibrated with high-T mafic liquids (Ionov et al., 2005c). This may indicate that the high-T melt metasomatism in the LW series rocks was followed by percolation of low-T, Na-rich melts or fluids. It is likely that after the sources of high-T

mafic melts were exhausted, the upward migration of low-T melts and fluids from sub-lithospheric mantle (Fig. 15) continued for some time both in the LH and the LW rocks to make their trace element signatures closer to each other. Later on, the percolation front of the low-T melts and fluids must have receded from the top to the bottom of the mantle section as the hypothetical sub-lithospheric source of heat and fluids cooled further and finally ceased to exist.

At that latter stage when percolation weakened and stopped, entrapment and solidification of residual melts enriched in alkalis and volatiles could have formed accessory amph and phl. The trapped melt may also contribute to whole-rock enrichments in highly incompatible elements, which could be as important as equilibration of peridotite minerals with percolating melts. For example, in situ crystallisation of 1% of a liquid containing 50 ppm La (like in host basalts, Table 8) provides 0.5 ppm La to the whole-rock budget of peridotite, i.e., several times more than the share of 5% cpx equilibrated with the same liquid ($^{cpx/melt}D_{La} = 0.054$; $La_{Cpx} = 2.7$ ppm and $La_{WR} = 0.13$ ppm). The amount of trapped liquid can be roughly estimated from whole-rock abundances of elements with very low partition coefficients in residual minerals, like Rb (assuming $^{rock/melt}D_{Rb} = 0$). A plot of Rb vs. La (Fig. 10H) shows a positive correlation for P-poor ($P_2O_5 <$ 0.06%) Tok peridotites extending to cumulate xenolith 8–14. Attributing all Rb to a trapped metasomatic liquid with 30 ppm Rb (like in host basalts) yields 2–6% of the trapped liquid for the cumulates, 2–4% for phl-bearing rocks with 0.8–1.2 ppm Rb and 0.3–1.5% for other xenoliths. These values should be considered as upper limits because major minerals may contain some Rb and because Rb abundances in the hypothetical residual fluids are likely to be higher than in the host basalt (Fig. 12B). Thus, the porosity was probably quite low near the end of the major percolation event.

Overall, the major melt percolation event inferred from chemical data on Tok peridotites encompassed the whole lithospheric mantle section "sampled" by the xenoliths (likely in the depth range 40–60 km; Ionov et al., 2005e) and was long-living. It probably started with migration of high-T mafic melts from a sub-lithospheric source along high-permeability zones to form LW series rocks and was followed by frontal upward percolation of low-T melts and fluids. The total duration of the event may have been on the order of millions or tens of millions of years considering the time required first to heat the cold lithospheric mantle to enable melt percolation and then for the thermal anomaly to dissipate by conductive heat loss (Rudnick, 1998; and references therein).

Theoretical modelling (e.g., Bedini et al., 1997; Vernières et al., 1997) has so far focused on the "prograde" stage of large-scale percolation events, which produces strong LREE enrichments near the percolation front and equilibration with the initial melt closer to the melt source, in line with much of our data on the Tok xenoliths (Figs. 14A and 15). Here, we would like to also draw attention to the "retrograde" stage of such events, i.e., during thermal relaxation of the metasomatic system when the source of heat and melt becomes progressively weaker. The melt/fluid percolation from the source upwards at that stage is not likely to cease abruptly but would rather decrease gradually; as a result the percolation front would reverse and migrate back gradually to pass through the section earlier affected by the "prograde" stage of the same event. It is not likely that chemical signatures of the "prograde" metasomatism can be erased or significantly overprinted at the "retrograde" stage because of smaller melt volumes, lower porosity and shorter duration of the latter stage. However, this relaxation event may be responsible for minor local enrichments with specific trace element signatures and chemical heterogeneities in the xenoliths. The appearance of cpx generations with a range of Na, LREE and HFSE (Figs. 1A and B, 4F, 5 and 7A) is most likely related to that event. These and other late-stage processes will be further considered in the next section.

5.5.2. Late-stage enrichments by small-volume alkali- and P-rich melts

As discussed above, small-volume melts enriched in alkalis, phosphorus and LREE may have been important enrichment agents near the percolation front during the inferred main metasomatic event. The majority of Tok peridotites with moderate contents of K_2O and P_2O_5 define a positive K–P correlation (Fig. 14B) indicating metasomatism by a series of melts with gradually increasing contents of alkalis and phosphorus; such melts could have formed by progressive fractionation of an initial basaltic liquid at decreasing volume (e.g., Bodinier et al., 2004). A smaller number of Tok xenoliths, however, define two distinct trends in Fig. 14B: one with high P_2O_5 (>0.1%) at low to moderate K_2O and another one (LW series only) of high K_2O (>0.1%) at moderate P_2O_5. Those relationships may be explained by formation of a distinct P_2O_5-rich melt or fluid phase as the ultimate differentiation product of an initial volatile-bearing silicate liquid following precipitation of cpx, amph and phl (the latter may be a reason for local enrichments in K).

It is likely that carbonates or CO_2 were major components in the P_2O_5-rich phase as proposed earlier (e.g., Bedini et al., 1997; Ionov et al., 2002; Bodinier et al., 2004). The combination of high P_2O_5 and La with low HFSE (as well as low Rb; Fig. 10H) in the phosphate-rich Tok xenoliths cannot be due to unusually high proportion of trapped silicate melt and thus provides another argument for a separate metasomatic fluid rich in LREE and P_2O_5. Cumulate xenoliths, which contain abundant crystallisation products of a trapped silicate melt (Figs. 2G and H in Ionov et al., 2005c), have lower La and P_2O_5 than the La-rich peridotites (Fig. 10). Negative anomalies of Zr, Hf and Nb in the P_2O_5-rich rocks (Figs. 3D and 9F) can be explained by lower solubilities of HFSE in carbonate-rich melts coexisting with silicate melts (Ionov et al., 2002; Bodinier et al., 2004; and references therein).

As mentioned above, a combination of high La/Yb with low Ti/Eu (Fig. 10I), negative HFSE anomalies, high Zr/Hf and the presence of apatite were proposed as geochemical signatures of "carbonatite" metasomatism (Green and Wallace, 1988; Yaxley et al., 1991; Hauri et al., 1993; Ionov et al., 1993; Rudnick et al., 1993). This study further indicates that such features may not require a distinct carbonatite source but can result from strong fractionation of volatile-bearing basaltic liquids (e.g., Laurora et al., 2001; Bodinier et al., 2004; Rivalenti et al., 2004). No carbonates have been found in Tok xenoliths in spite of extensive search with optical microscopy and EPMA; the search included opx-free LW series wehrlites, in which carbonates can be stable in shallow mantle even at moderately high-*T*'s (Dalton and Wood, 1993). This may indicate that the hypothetical late-stage P_2O_5-rich metasomatic media were silicate melts or fluids rich in carbonates or CO_2 rather than true carbonatites. Phosphates commonly occur on the walls of empty cavities (Figs. 1D and 2D) and sometimes form spongy aggregates with abundant empty vesicles (Fig. 1C); those cavities must have been filled with CO_2 produced in the fluid–rock reaction; CO_2 later escaped.

The timing and nature of strong enrichments in LREE and phosphorus may not be the same for all the xenoliths. As discussed in the previous section, we believe that strong LREE-enrichments in the cpx, apparently equilibrated with coexisting phosphates (e.g., 5–3 in Fig. 11A), were produced near the percolation front during the major percolation event (Figs. 14A and 15). In other xenoliths, like 10–11, cpx with concave-upward REE pattern and $La/Nd_{PM} < 1$ coexists with LREE-enriched apatite (Fig. 11B); the latter is not equilibrated with the cpx and hence may have formed from a genetically unrelated P_2O_5-rich fluid in a later event. Moreover, infiltration of any metasomatic fluid could probably mobilise and redistribute phosphates and alkali-rich phases precipitated by previous events.

Several lines of evidence indicate that small-scale metasomatic events continued in the Tok mantle until the eruption of quaternary basaltic magmas hosting the xenoliths. A few xenoliths contain quenched cryptocrystalline materials with empty vesicles (Fig. 8). Those materials must have formed from interstitial volatile-rich melts, most likely when they abruptly lost their volatile components during the entrainment of the xenoliths in the magma. Because no amph and phl have been found in association with those or other late-stage materials in the Tok xenoliths, the evaded volatile phase most likely consisted of CO_2. Similar origins can also be envisaged for fine-grained veins and pockets of interstitial feldspar with micro-phenocrysts of olivine, cpx, spl and phosphates (Figs. 2B–D). Such aggregates may have formed from similar volatile-rich melts, which had a little more time to solidify, probably because they lost their volatile components more gradually (e.g., due to rock micro-fracturing before the eruption) than the quenched cryptocrystalline materials.

Another important piece of evidence for migration of CO_2-rich, water-poor fluids in the Tok mantle shortly before the eruption of quaternary basalts is the breakdown of "hydrous" amph and phl in the xenoliths (Figs. 1 and 2). We emphasize that the breakdown products contain no glass and that there is no evidence to relate their formation to heating and pressure release during the transport in the magma (e.g., amph and phl in some xenoliths are well preserved; Fig. 3f in Ionov et al., 2005e). Rather, the breakdown of the hydroxyl-bearing silicates could be caused by infiltration of fluids with low water activity (e.g., due to low H_2O/CO_2) such that amph and phl became nearly instantly unstable and turned into fine-grained aggregates of "anhydrous" phases, as proposed earlier for other xenolith suites from the Russian far east by Ionov et al. (1999). The discovery of "anhydrous" whitlockite coexisting with apatite in some of those samples corroborates low water activity in the fluid. The unusual Ba–Ti-rich silicate (Fig. 2E and Table 1) found in some xenoliths must have formed after Ba-rich phl. As discussed above, the amph and phl in the Tok peridotites may have formed at the relaxation stage of the main melt percolation event due to entrapment of residual hydrous melts or fluids produced by fractionation of initial water-bearing basaltic melts. Thus, the essentially "dry" late-stage fluids are chemically different from the fluids that previously precipitated amph and phl and probably came from a genetically distinct source. The latter may be related to the quaternary alkali basaltic volcanism. It is possible that there was a significant time lap between the complete end (including the "retrograde" stage) of the inferred main metasomatic event and the infiltration of the late-stage water-poor fluids.

5.5.3. Tectonic settings and sources of metasomatism

A major inference of this study is that widespread metasomatism in the refractory Tok mantle was caused by long-term upward melt percolation, which encompassed the whole lithospheric section represented by the xenoliths. Such an event requires a strong and long-living source of heat and melts. Ionov et al. (2005e) noted that equilibration *T*'s in the shallow Tok mantle are much higher than at the same level in the centre of the craton and speculated that the cratonic keel at the bottom of the Tok lithosphere may have been delaminated. If the latter is correct, the delamination of the lower lithosphere could have supplied the heat and melts for the metasomatism in the overlying shallow mantle. The age of the main metasomatic event is not known, but it cannot be very young considering a long time required for a mantle section $\geqslant 20$ km thick to cool from sub-magmatic *T*'s ($\sim$1300 °C for LW series rocks) to 900–1000 °C by conductive heat loss. Hence, the main metasomatic event is not related to the late-Cenozoic basaltic volcanism.

A major tectono-magmatic event involving alkali magmatism and graben formation took place at the SE margin of the Siberian craton in late-Mesozoic–early Cenozoic (Zonenshain et al., 1990). The event was likely related to

concomitant subduction in the adjacent paleo-Pacific oceanic basin and could cause delamination of the lower lithosphere and supply the heat and fluids for the major metasomatic event in the shallow Tok mantle. Several features inferred for that metasomatic event may be consistent with a subduction-related source, like strong LREE enrichments, negative Ti anomalies and (less common) Zr and Hf anomalies as well as precipitation of water-bearing amph and phl from residual melts. Those events in the Tok mantle could be roughly contemporaneous with widespread delamination of the Archean lithospheric mantle and metasomatism inferred for the nearby North China craton from xenolith data (e.g., Menzies et al., 1993; Xu et al., 2003).

Some small-scale, late-stage metasomatic features in Tok xenoliths are contemporaneous with Cenozoic basaltic volcanism and could be caused by fluids related to that volcanism. Those fluids had low water activity (as indicated by breakdown of previously formed amph and phl and precipitation of whitlockite), unlike the melts responsible for the earlier large-scale metasomatic event. Studies of volcanic rocks from the Russian far east south of Tok (Okamura et al., 2005) have shown that a significant and abrupt change in their geochemical signatures from subduction-related to asthenospheric took place between the early and late-Cenozoic. Detailed in situ studies are necessary to further constrain the role of the latest metasomatism in the Tok mantle. It is possible that it mainly remobilised some components (alkalis and phosphates) deposited by earlier events.

6. Summary

(1) The lithospheric mantle beneath Tok consists mainly of olivine-rich spinel peridotites initially produced by high degrees of melt extraction. These rocks experienced widespread metasomatic re-working, which largely erased the geochemical record of previous melting events and imparted mineralogical and trace element signatures of enriched melts/fluids.

(2) Cpx in the olivine-rich Tok peridotites have PM-normalised element patterns ranging from dominant convex-upward (indicative of equilibration with evolved silicate liquids) to LREE-enriched; the latter are most common in the shallow mantle. We infer that the mantle section represented by the xenoliths experienced a large-scale metasomatic event produced by upward migration of alkali-rich basaltic melts. Chromatographic fractionation and fractional crystallisation of the melts close to the percolation front produced strong LREE-enrichments.

(3) The percolating melts progressively evolved from basaltic liquids to low-T, alkali-rich silicate and then CO_2- and P_2O_5-rich derivatives. The latter have geochemical features often attributed to "carbonatite" metasomatism. The percolation front migrated downwards at the "retrograde" stage of the event. Trapped residual melts formed accessory amph and phl and cpx generations with a range of Na and trace element abundances.

(4) The initial silicate melts responsible for the main, large-scale metasomatic event were enriched in LREE and depleted in Ti. Their sources may have been related to late-Mesozoic–early Cenozoic subduction in the paleo-Pacific ocean basin. Shortly before the entrainment into quaternary basaltic magma the xenoliths were infiltrated by fluids, which triggered formation of interstitial materials containing alkali feldspar and Ti-rich oxides.

(5) In addition to apatite, many Tok xenoliths contain whitlockite—an "anhydrous" and halogen-poor phosphate, which is common in meteorites and lunar rocks, but has not been reported as yet from other terrestrial mantle samples. The presence of whitlockite, together with replacement of amph and phl by "anhydrous" assemblages, indicates low activities of water and halogens in the fluids related to the last metasomatic episode.

Acknowledgments

D.A.I. thanks Al Hofmann for support at Mainz and V. Prikhodko (ITIG, Far Eastern Branch of the Russian Academy of Sciences) for help with fieldwork in Siberia. Analytical assistance was provided by B. Boyer, I. Chanefo, F. Keller, L. Nasdala and B. Stoll. D.A.I. acknowledges a visiting research scientist position at Université Blaise Pascal in 2000 and a visiting professor position at Université de Grenoble in 2002. Editorial handling by F. Frey and comments of H.-G. Stosch and an anonymous reviewer are appreciated.

Associate editor: Frederick A. Frey

References

Bedini, R.M., Bodinier, J.-L., 1999. Distribution of incompatible trace elements between the constituents of spinel peridotite xenoliths: ICP-MS data from the East African rift. *Geochim. Cosmochim. Acta* **63**, 3883–3900.

Bedini, R.M., Bodinier, J.-L., Dautria, J.-M., Morten, L., 1997. Evolution of LILE-enriched small melt fractions in the lithospheric mantle: a case study from the East African Rift. *Earth Planet. Sci. Lett.* **153**, 67–83.

Blundy, J.D., Robinson, J.A.C., Wood, B.J., 1998. Heavy REE are compatible in clinopyroxene on the spinel lherzolite solidus. *Earth Planet. Sci. Lett.* **160**, 493–504.

Bodinier, J.-L., Godard, M., 2003. Orogenic, ophiolitic and abyssal peridotites. In: Carlson, R.W. (Ed.), *Treatise on Geochemistry. Vol. 2. The Mantle and Core*. Elsevier, pp. 103–170.

Bodinier, J.-L., Menzies, M.A., Shimizu, N., Frey, F.A., McPherson, E., 2004. Silicate, hydrous and carbonate metasomatism at Lherz, France: contemporaneous derivatives of silicate melt–harzburgite reaction. *J. Petrol.* **45**, 299–320.

Bodinier, J.-L., Merlet, C., Bedini, R.M., Simien, F., Remaidi, M., Garrido, C.J., 1996. Distribution of niobium, tantalum, and other highly incompatible trace elements in the lithospheric mantle: the spinel paradox. *Geochim. Cosmochim. Acta* **60**, 545–550.

Bodinier, J.-L., Vasseur, G., Vernières, J., Dupuy, C., Fabriès, J., 1990. Mechanisms of mantle metasomatism: geochemical evidence from the Lherz orogenic peridotite. *J. Petrol.* **31**, 597–628.

Bottazzi, P., Ottolini, L., Vannucci, R., Zanetti, A., 1994. An accurate procedure for the quantification of rare earth elements in silicates. In: Benninghoven, A., Nihei, Y., Shimizu, R., Werner, H.V. (Eds.), *Secondary Ion Mass Spectrometry, SIMS IX*. J. Wiley, pp. 927–930.

Brey, G.P., Köhler, T., 1990. Geothermobarometry in four-phase lherzolites II. New thermobarometers, and practical assessment of existing thermobarometers. *J. Petrol.* **31**, 1353–1378.

Chazot, G., Menzies, M., Harte, B., 1996. Determination of partition coefficients between apatite, clinopyroxene, amphibole, and melt in natural spinel lherzolites from Yemen: implications for wet melting of the lithospheric mantle. *Geochim. Cosmochim. Acta* **60**, 423–437.

Dalton, J.A., Wood, B.J., 1993. The partitioning of Fe and Mg between olivine and carbonate and the stability of carbonate under mantle conditions. *Contrib. Mineral. Petrol.* **114**, 501–509.

Eggins, S.M., 2003. Laser ablation ICP-MS analysis of geological materials prepared as lithium borate glasses. *Geostand. Newslett.* **27**, 147–162.

Eggins, S.M., Woodhead, J.D., Kinsley, L.P.J., Mortimer, G.E., Sylvester, P., McCulloch, M.T., Hergt, J.M., Handler, M.R., 1997. A simple method for the precise determination of $\geqslant$40 trace elements in geological samples by ICP-MS using enriched isotope internal stardardisation. *Chem. Geol.* **134**, 311–326.

Gaetani, G.A., 2004. The influence of melt structure on trace element partitioning near the peridotite solidus. *Contrib. Mineral. Petrol.* **147**, 511–527.

Green, D.H., Wallace, M.E., 1988. Mantle metasomatism by ephemeral carbonatite melts. *Nature* **336**, 459–462.

Grégoire, M., Moine, B.N., O'Reilly, S.Y., Cottin, J.Y., Giret, A., 2000. Trace element residence and partitioning in mantle xenoliths metasomatised by highly alkaline, silicate- and carbonate-rich melts (Kerguelen Islands, Indian Ocean). *J. Petrol.* **41**, 477–509.

Grégoire, M., Tinguely, C., Bell, D.R., Roex, A.P.l., 2005. Spinel lherzolite xenoliths from the Premier kimberlite (Kaapvaal craton, South Africa): Nature and evolution of the shallow upper mantle beneath the Bushveld complex. *Lithos* **84**, 185–205.

Hart, S.R., Dunn, T., 1993. Experimental cpx/melt partitioning of 24 trace elements. *Contrib. Mineral. Petrol.* **113**, 1–8.

Harte, B., Hunter, R.H., Kinny, P.D., 1993. Melt geometry, movement and crystallization, in relation to mantle dykes, veins and metasomatism. *Philos. Trans. R. Soc. Lond. A* **342**, 1–21.

Hauri, E.H., Shimizu, N., Dieu, J.J., Hart, S.R., 1993. Evidence for hotspot-related carbonatite metasomatism in the oceanic upper mantle. *Nature* **365**, 221–227.

Hellebrand, E., Snow, J.E., 2003. Deep melting and sodic metasomatism underneath the highly oblique-spreading Lena Trough (Arctic Ocean). *Earth Planet. Sci. Lett.* **216**, 283–299.

Hellebrand, E., Snow, J.E., Dick, H.J.B., Hofmann, A.W., 2001. Coupled major and trace elements as indicators of the extent of melting in mid-ocean-ridge peridotites. *Nature* **410**, 677–681.

Hellebrand, E., Snow, J.E., Hoppe, P., Hofmann, A.W., 2002. Garnet-field melting and late-stage refertilization in 'residual' abyssal peridotites from the Central Indian Ridge. *J. Petrol.* **43**, 2305–2338.

Hofmann, A.W., 1988. Chemical differentiation of the Earth: the relationship between mantle, continental crust, and oceanic crust. *Earth Planet. Sci. Lett.* **90**, 297–314.

Ionov, D.A., Ashchepkov, I., Jagoutz, E., 2005a. The provenance of fertile off-craton lithospheric mantle: Sr–Nd isotope and chemical composition of garnet and spinel peridotite xenoliths from Vitim, Siberia. *Chem. Geol.* **217**, 41–75.

Ionov, D.A., Blichert-Toft, J., Weis, D., 2005b. Hf isotope compositions and HREE variations in off-craton garnet and spinel peridotite xenoliths from central Asia. *Geochim. Cosmochim. Acta* **69**, 2399–2418.

Ionov, D.A., Bodinier, J.-L., Mukasa, S.B., Zanetti, A., 2002. Mechanisms and sources of mantle metasomatism: major and trace element compositions of peridotite xenoliths from Spitsbergen in the context of numerical modeling. *J. Petrol.* **43**, 2219–2259.

Ionov, D.A., Chanefo, I., Bodinier, J.-L., 2005c. Origin of Fe-rich lherzolites and wehrlites from Tok, SE Siberia by reactive melt percolation in refractory mantle peridotites. *Contrib. Mineral. Petrol.* **150**, 335–353.

Ionov, D.A., Dupuy, C., O'Reilly, S.Y., Kopylova, M.G., Genshaft, Y.S., 1993. Carbonated peridotite xenoliths from Spitsbergen: implications for trace element signature of mantle carbonate metasomatism. *Earth Planet. Sci. Lett.* **119**, 283–297.

Ionov, D.A., Grégoire, M., Prikhodko, V.S., 1999. Feldspar–Ti-oxide metasomatism in off-cratonic continental and oceanic upper mantle. *Earth Planet. Sci. Lett.* **165**, 37–44.

Ionov, D.A., Hofmann, A.W., 1995. Nb–Ta-rich mantle amphiboles and micas: implications for subduction-related metasomatic trace element fractionations. *Earth Planet. Sci. Lett.* **131**, 341–356.

Ionov, D.A., Hofmann, A.W., Gurenko, A., Hellebrand, E., Montagnac, G., Gillet, P., 2005d. Whitlockite and Ba,Ti-rich mica in Siberian xenoliths indicate 'dry' conditions in parts of terrestrial mantle. *Geochim. Cosmochim. Acta* **69** (10, supplement 1), , abstract EGU05-A-03535.

Ionov, D.A., Hofmann, A.W., Shimizu, N., 1994. Metasomatism-induced melting in mantle xenoliths from Mongolia. *J. Petrol.* **35**, 753–785.

Ionov, D.A., O'Reilly, S.Y., Ashchepkov, I.V., 1995a. Feldspar-bearing lherzolite xenoliths in alkali basalts from Hamar-Daban, southern Baikal region, Russia. *Contrib. Mineral. Petrol.* **122**, 174–190.

Ionov, D.A., O'Reilly, S.Y., Griffin, W.L., 1997. Volatile-bearing minerals and lithophile trace elements in the upper mantle. *Chem. Geol.* **141**, 153–184.

Ionov, D.A., Prikhodko, V.S., Bodinier, J.-L., Sobolev, A.V., Weis, D., 2005e. Lithospheric mantle beneath the south-eastern Siberian craton: petrology of peridotite xenoliths in basalts from the Tokinsky Stanovik. *Contrib. Mineral. Petrol.* **149**, 647–665.

Ionov, D.A., Prikhodko, V.S., O'Reilly, S.Y., 1995b. Peridotite xenoliths in alkali basalts from the Sikhote-Alin, southeastern Siberia, Russia: trace element signatures of mantle beneath a convergent continental margin. *Chem. Geol.* **120**, 275–294.

Johnson, K.T.M., Dick, H.J.B., Shimizu, N., 1990. Melting in the oceanic upper mantle: an ion probe study of diopsides in abyssal peridotites. *J. Geophys. Res.* **95**, 2661–2678.

Kalfoun, F., Ionov, D., Merlet, C., 2002. HFSE residence and Nb–Ta ratios in metasomatised, rutile-bearing mantle peridotites. *Earth Planet. Sci. Lett.* **199**, 49–65.

Koga, K., Kelemen, P., Shimizu, N., 2001. Petrogenesis of the crust–mantle transition zone and the origin of lower crustal wehrlite in the Oman ophiolite. *Geochem. Geophys. Geosyst.* **2**, doi:10.1029/2000GC000132.

Laurora, A., Mazzucchelli, M., Rivalenti, G., Vannucci, R., Zanetti, A., Barbieri, M.A., Cingolani, C.A., 2001. Metasomatism and melting in carbonated peridotite xenoliths from the mantle wedge: The Gobernador Gregores case (southern Patagonia). *J. Petrol.* **42**, 69–87.

Mattielli, N., Weis, D., Scoates, J.S., Shimizu, N., Mennessier, J.-P., Grégoire, M., Cottin, J.-Y., Giret, A., 1999. Evolution of heterogeneous lithospheric mantle in a plume environment beneath the Kerguelen Archipelago. *J. Petrol.* **40**, 1721–1744.

McDade, P., Blundy, J.D., Wood, B.J., 2003. Trace element partitioning on the Tinaquillo Lherzolite solidus at 1.5 GPa. *Phys. Earth Planet. Interiors* **139**, 129–147.

McDonough, W.F., Frey, F.A., 1989. Rare earth elements in upper mantle rocks. In: Lipin, B.R., McKay, G.A. (Eds.), *Geochemistry and Mineralogy of Rare Earth Elements*. Mineral. Soc. Amer., pp. 99–145.

Menzies, M.A., Fan, W., Zhang, M., 1993. Paleozoic and Cenozoic lithoprobes and the loss of >120 km of Archaean lithosphere, Sino-Korean craton. *Geol. Soc. Lond. Spec. Publ.* **76**, 71–81.

Merlet, C., 1994. An accurate computer correction program for quantitative electron probe microanalysis. *Mikrochim. Acta* **114/115**, 363–376.

Navon, O., Stolper, E., 1987. Geochemical consequences of melt percolation: the upper mantle as a chromatographic column. *J. Geol.* **95**, 285–307.

Neumann, E.-R., Wulff-Pedersen, E., Pearson, N.J., Spenser, E.A., 2002. Mantle xenoliths from Tenerife (Canary Islands): evidence for reactions between mantle peridotites and silicic carbonatite melts inducing Ca metasomatism. *J. Petrol.* **43**, 825–857.

Norman, M.D., 1998. Melting and metasomatism in the continental lithosphere: laser ablation ICPMS analyses of minerals in spinel lherzolites from eastern Australia. *Contrib. Mineral. Petrol.* **130**, 240–255.

Okamura, S., Arculus, R.J., Martynov, Y.A., 2005. Cenozoic magmatism of the North-Eastern Eurasian margin: the role of lithosphere versus asthenosphere. *J. Petrol.* **46**, 221–253.

Pearce, N.J.G., Perkins, W.T., Westgate, J.A., Gorton, M.P., Jackson, S.E., Neal, S.R., Chenery, S.P., 1997. A compilation of new and published major and trace element data for NIST SRM 610 and NIST SRM 612 glass reference materials. *Geostand. Newslett.* **21**, 115–144.

Pearson, D.G., Canil, D., Shirey, S.B., 2003. Mantle samples included in volcanic rocks: xenoliths and diamonds. In: Carlson, R.W. (Ed.), *Treatise on Geochemistry. Vol. 2. The Mantle and Core*. Elsevier, NY, pp. 171–276.

Peslier, A.H., Francis, D., Ludden, J., 2002. The lithospheric mantle beneath continental margins: melting and melt–rock reaction in Canadian Cordillera xenoliths. *J. Petrol.* **43**, 2013–2047.

Raczek, I., Stoll, B., Hofmann, A.W., Jochum, K.P., 2001. High-precision trace element data for the USGS reference materials BCR-1, BCR-2, BHVO-1, BHVO-2, AGV-1, AGV-2, DTS-1, DTS-2, GSP-1 and GSP-2 by ID-TIMS and MIC-SSMS. *Geostand. Newslett.* **25**, 77–86.

Rivalenti, G., Zanetti, A., Mazzucchelli, M., Vannucci, R., Cingolani, C.A., 2004. Equivocal carbonatite markers in the mantle xenoliths of the Patagonia backarc: the Gobernador Gregores case (Santa Cruz Province, Argentina). *Contrib. Mineral. Petrol.* **147**, 647–670.

Ross, K., Elthon, D., 1997. Extreme incompatible trace-element depletion of diopside in residual mantle from south of the Kane Fracture Zone. *Proc. ODP Sci. Res.* **153**, 277–284.

Rudnick, R.L., 1998. Thermal structure, thickness and composition of continental lithosphere. *Chem. Geol.* **145**, 395–411.

Rudnick, R.L., McDonough, W.F., Chappell, B.C., 1993. Carbonatite metasomatism in the northern Tanzanian mantle. *Earth Planet. Sci. Lett.* **114**, 463–475.

Stosch, H.-G., Lugmair, G.W., Kovalenko, V.I., 1986. Spinel peridotite xenoliths from the Tariat Depression, Mongolia. II: Geochemistry and Nd and Sr isotopic composition and their implications for the evolution of the subcontinental lithosphere. *Geochim. Cosmochim. Acta* **50**, 2601–2614.

Takazawa, E., Frey, F.A., Shimizu, N., Obata, M., 2000. Whole rock compositional variations in an upper mantle peridotite (Horoman, Hokkaido, Japan): are they consistent with a partial melting process. *Geochim. Cosmochim. Acta* **64**, 695–716.

Tichomirowa, M., Whitehouse, M.J., Nasdala, L., 2005. Resorption, growth, solid state recrystallisation, and annealing of granulite facies zircon–a case study from the Central Erzgebirge, Bohemian Massif. *Lithos* **82**, 25–50.

Toramaru, A., Fujii, N., 1986. Connectivity of melt phase in a partially molten peridotite. *J. Geophys. Res.* **91**, 9239–9252.

Vernières, J., Godard, M., Bodinier, J.-L., 1997. A plate model for the simulation of trace element fractionation during partial melting and magma transport in the Earth's upper mantle. *J. Geophys. Res.* **102**, 24771–24784.

Wiechert, U., Ionov, D.A., Wedepohl, K.H., 1997. Spinel peridotite xenoliths from the Atsagin–Dush volcano, Dariganga lava plateau, Mongolia: a record of partial melting and cryptic metasomatism in the upper mantle. *Contrib. Mineral. Petrol.* **126**, 345–364.

Witt-Eickschen, G., O'Neill, H.S.C., 2005. The effect of temperature on the equilibrium distribution of trace elements between clinopyroxene, orthopyroxene, olivine and spinel in upper mantle peridotite. *Chem. Geol.* **221**, 65–101.

Witt-Eickschen, G., Seck, H.A., Mezger, K., Eggins, S.M., Altherr, R., 2003. Lithospheric mantle evolution beneath the Eifel (Germany): constraints from Sr–Nd–Pb isotopes and trace element abundances in spinel peridotite and pyroxenite xenoliths. *J. Petrol.* **44**, 1077–1095.

Xu, Y.-G., Menzies, M.A., Thirlwall, M.F., Huang, X.-L., Liu, Y., Chen, X.-M., 2003. "Reactive" harzburgites from Huinan, NE China: products of the lithosphere–asthenosphere interaction during lithospheric thinning? *Geochim. Cosmochim. Acta* **67**, 487–505.

Yaxley, G.M., Crawford, A.J., Green, D.H., 1991. Evidence for carbonatite metasomatism in spinel peridotite xenoliths from western Victoria, Australia. *Earth Planet. Sci. Lett.* **107**, 305–317.

Yaxley, G.M., Green, D.H., Kamenetsky, V., 1998. Carbonate metasomatism in the southeastern Australian lithosphere. *J. Petrol.* **39**, 1917–1931.

Zonenshain, L.P., Kuzmin, M.I., Natapov, L.M., 1990. In: *Geology of the USSR: A Plate Tectonic Synthesis*. Am. Geophys. Union Geodynamics Ser. 21., Washington, DC, p. 242.